

## Dynamically Tagged Groups of Metal-Poor Stars II. The Radial Velocity Experiment Data Release 6

DEREK SHANK <sup>1,2</sup> DANTE KOMATER <sup>1</sup> TIMOTHY C. BEERS <sup>1,2</sup> VINICIUS M. PLACCO <sup>3</sup> AND YANG HUANG <sup>4</sup>

<sup>1</sup>*Department of Physics, University of Notre Dame, Notre Dame, IN 46556, USA*

<sup>2</sup>*Joint Institute for Nuclear Astrophysics – Center for the Evolution of the Elements (JINA-CEE), USA*

<sup>3</sup>*NSF’s NOIRLab, 950 N. Cherry Ave., Tucson, AZ 85719, USA*

<sup>4</sup>*South-Western Institute for Astronomy Research, Yunnan University, Kunming 650500, People’s Republic of China*

(Dated: January 21, 2022)

### ABSTRACT

Orbital characteristics based on Gaia Early Data Release 3 astrometric parameters are analyzed for  $\sim 8,000$  metal-poor stars ( $[\text{Fe}/\text{H}] \leq -0.8$ ) compiled from the RADial Velocity Experiment (RAVE) Data Release 6. Selected as metal-poor candidates based on broadband photometry, RAVE collected moderate-resolution ( $R \sim 7,500$ ) spectra in the region of the Ca triplet for these stars. About 20% of the stars in this sample also have medium-resolution ( $1,200 \lesssim R \lesssim 2,000$ ) validation spectra obtained over a four-year campaign from 2014 to 2017 with a variety of telescopes. We match the candidate stars to photometric metallicity determinations from the Huang et al. recalibration of the Sky Mapper Southern Survey Data Release 2. We obtain dynamical clusters of these stars from the orbital energy and cylindrical actions using the HDBSCAN unsupervised learning algorithm. We identify 179 Dynamically Tagged Groups (DTGs) with between 5 and 35 members; 67 DTGs have at least 10 member stars. Milky Way (MW) substructures such as Gaia-Sausage-Enceladus, the Metal-Weak Thick Disk, the Splashed Disk, Thamnos, the Helmi Stream, and LMS-1 (Wukong) are identified. Associations with MW globular clusters are determined for 10 DTGs; no recognized MW dwarf galaxies were associated with any of our DTGs. Previously identified dynamical groups are also associated with our DTGs, with emphasis placed on their structural determination and possible new identifications. We identify chemically peculiar stars as members of several DTGs; we find 22 DTGs that are associated with  $r$ -process-enhanced stars. Carbon-enhanced metal-poor (CEMP) stars are identified among the targets with available spectroscopy, and we assign these to morphological groups following the approach given by Yoon et al.

*Keywords:* Milky Way dynamics (1051), Galaxy dynamics (591), Galactic archaeology (2178), Milky Way evolution (1052), Milky Way formation (1053), Milky Way stellar halo (1060)

### 1. INTRODUCTION

Large-scale spectroscopic surveys conducted over the last few decades have allowed the structure, assembly, and chemical-evolution history of the Milky Way (MW) to be explored in great detail (York et al. 2000; Yanny et al. 2009; Cui et al. 2012). The spectra from such surveys provide important information about stellar atmospheres, in particular their chemical abundances, an important tool for determining the origin and evolution of the elements in the stellar populations of the Galaxy. The collected spectra can also provide radial velocity measurements, which are used as one of the 6-D astrometric parameters (along with position, distance, and

proper motions) to derive the orbits of stars in a selected gravitational potential.

The Radial Velocity Experiment (RAVE; Steinmetz et al. 2006) is one of the largest contributors of such information. In the newest RAVE Data Release 6 (DR6; Steinmetz et al. 2020a) there are  $\sim 450,000$  unique stellar objects with radial velocities available, with 95% having an accuracy better than  $4.0 \text{ km s}^{-1}$ . With such a large and homogeneous set of radial velocities available, RAVE provides the opportunity to study the MW through both their dynamics and chemical compositions. One of the first uses of RAVE to study MW dynamics was by Seabroke et al. (2008), who determined that there were no vertical tidal streams asso-

ciated within the Solar Neighborhood, the region surveyed by RAVE Data Release 1 (DR1; Steinmetz et al. 2006). Also using RAVE DR1, Klement et al. (2008) discovered a new radial stream, while recovering previously known streams such as the Helmi Stream (Helmi et al. 1999). The stellar parameters obtained by RAVE have allowed astronomers to discover metal-poor stars ( $[\text{Fe}/\text{H}]^1 \lesssim -1.0$ ), as first reported by Fulbright et al. (2010) using both DR1 and Data Release 2 (DR2; Zwitter et al. 2008).

Coşkunoglu et al. (2011, 2012), Bilir et al. (2012), Duran et al. (2013), and Karaali et al. (2014) employed kinematics and stellar parameters from RAVE to determine estimates of the Local Standard of Rest, radial and vertical metallicity gradients, and space velocity components for the thin and thick disk of the Galaxy. Antoja et al. (2012) was one of the first to probe beyond the Solar Neighborhood in search of kinematic groups using RAVE. These authors reidentified some known groups, such as Hercules, while also recovering new kinematic over-densities, revealing non-axisymmetric groups present in the MW. Utilizing the full RAVE Data Release 4 (DR4; Kordopatis et al. 2013), Binney et al. (2014) was able to compare the kinematics of stars within 2 kpc of the Sun to dynamical models, showing remarkable consistency for the velocity components of the sample.

The advent of Gaia (Gaia Collaboration et al. 2016a) has provided proper motions and parallax-based distances for an unprecedented number of stars. Using both Gaia Data Release 1 (DR1; Gaia Collaboration et al. 2016b) and RAVE DR4, Helmi et al. (2017) argued that the stellar halo was built solely by mergers and had a dominant retrograde-velocity component. Using the same data sets, Robin et al. (2017) were able to constrain the formation histories of the thin and thick disks. Recently, Li et al. (2020) employed RAVE Data Release 5 (DR5; Kunder et al. 2017) and Gaia Data Release 2 (DR2; Gaia Collaboration et al. 2018) to discover new structures in the MW using dynamical quantities such as the orbital energy and angular momentum, which offer insight into the structures’ origins.

When Galactic satellites are accreted and dispersed into the MW, the energies and dynamical actions of their member stars are expected to resemble those of their parent progenitor satellites (Helmi et al. 1999). The seminal work of Roederer et al. (2018) employed un-

supervised clustering algorithms, an approach that has proven crucial to determine structures in the MW that are not revealed through large-scale statistical sampling methods. These authors were able to collect 35 chemically peculiar ( $r$ -process-enhanced) stars and determine their orbits. With these data in hand, multiple clustering tools were applied to the orbital energy and actions to determine stars with similar orbital characteristics. This study revealed eight dynamical groupings comprising between two and four stars each. The small dispersion of each group’s metallicity was noted, and accounted for by reasoning that each group was associated with a unique satellite accretion event.

Yuan et al. (2020a) utilized the self-organizing map neural network routine StarGO (Yuan et al. 2018) on the Large Sky Area Multi-Object Fiber Spectroscopic Telescope (LAMOST; Cui et al. 2012) Data Release 3 (Li et al. 2018) stellar survey. These authors used StarGO to examine the very metal-poor ( $[\text{Fe}/\text{H}] \lesssim -1.8$ ) stars to seek dynamical clusters based on the derived energy, angular momentum, and polar and azimuthal ( $E, L, \theta, \phi$ ) parameters. From this prescription, the authors identified 57 dynamically tagged groups (DTGs), of which most were associated with GSE or Sequoia (Myeong et al. 2019), while 18 were new structures not previously associated with known large-scale substructures. Limberg et al. (2021a) constructed DTGs from metal-poor stars in the HK (Beers et al. 1985, 1992) and Hamburg/ESO (Christlieb et al. 2008) surveys using the Hierarchical Density-Based Spatial Clustering of Applications with Noise (HDBSCAN; Campello et al. 2013) algorithm over the orbital energy and cylindrical action space. Their clustering procedure was able to identify 38 DTGs, with 10 of those being newly identified substructures. Gudin et al. (2021) extended the work by Roederer et al. (2018), using a much larger sample of  $r$ -process-enhanced stars (see their Table 1 for definitions). Also utilizing the HDBSCAN algorithm, 30 Chemo-Dynamically Tagged Groups (CDTGs)<sup>2</sup> were discovered. Their analysis revealed statistically significant similarities in the dispersions of stellar metallicity, carbon abundance, and  $r$ -process-element ( $[\text{Sr}/\text{Fe}]$ ,  $[\text{Ba}/\text{Fe}]$ , and  $[\text{Eu}/\text{Fe}]$ ) abundances, strongly suggesting that these stars experienced similar chemical-evolution histories in their progenitor galaxies.

This work aims to analyze the DTGs present among stars in RAVE Data Release 6 (DR6; Steinmetz et al.

<sup>1</sup> The standard definition for an abundance ratio of an element in a star ( $\star$ ) compared to the Sun ( $\odot$ ) is given by  $[A/B] = (\log N_A/N_B)_\star - (\log N_A/N_B)_\odot$ , where  $N_A$  and  $N_B$  are the number densities of atoms for elements  $A$  and  $B$ .

<sup>2</sup> The distinction between CDTGs and DTGs is that the original stellar candidates of CDTGs are selected to be chemically peculiar in some fashion, while DTGs are selected from stars without detailed knowledge of their chemistry, other than  $[\text{Fe}/\text{H}]$ .

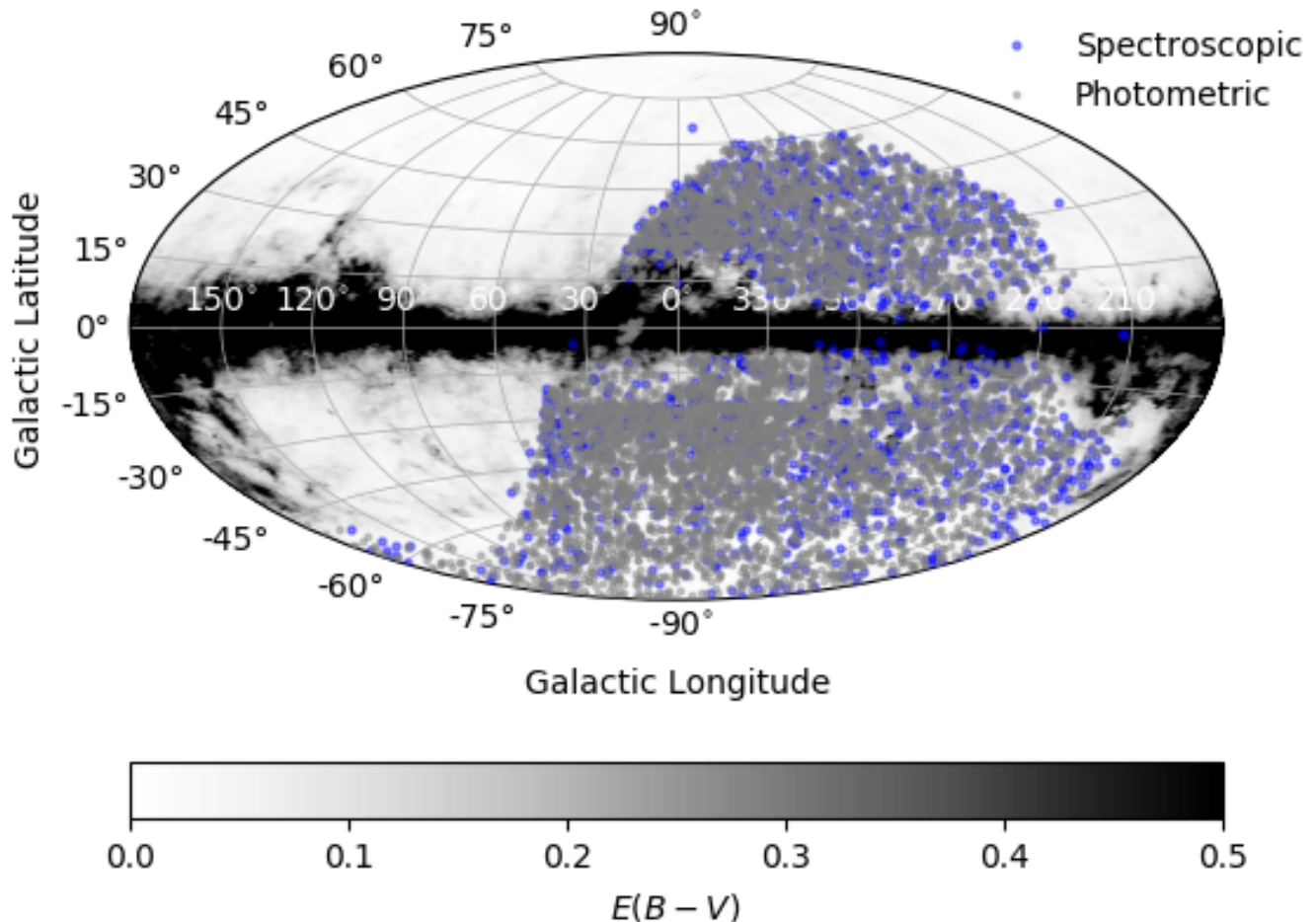


**Figure 1.** The Galactic positions of the Full Sample of RAVE DR6 stars with the spectroscopic subset shown as blue points and the photometric subset as gray points. The Galactic reddening map, taken from [Schlegel et al. \(1998\)](#), and recalibrated by [Schlafly & Finkbeiner \(2011\)](#), is shown in the background on a gray scale with darker regions corresponding to larger reddening.

2020a), focusing on metal-poor ( $[\text{Fe}/\text{H}] \leq -0.8$ ) stars. The procedures employed closely follow the work of [Shank et al. \(2021\)](#), hereafter referred to as Paper I in this series, which considered DTGs found in the sample of the Best & Brightest selection of [Schlaufman & Casey \(2014\)](#). The association of our identified DTGs with recognized Galactic substructures, previously known DTGs/CDTGs, globular clusters, and dwarf galaxies is explored, with the most interesting stellar populations being noted for future high-resolution follow-up studies.

This paper is outlined as follows. Section 2 describes the RAVE DR6 sample, along with their associated astrometric parameters and the dynamical parameters. The clustering procedure is outlined in Section 3. Section 4 explores the clusters and their association to known MW structures. Finally, Section 5 presents a short discussion and perspectives on future directions.

## 2. DATA

The RAVE DR6 survey ([Steinmetz et al. 2020a](#)) forms the basis for the compilation of our data set. We construct three samples, the Full Sample, the Initial Sample, and the Final Sample, which are described in the following sections.

### 2.1. Construction of the Full Sample

Of the 322,367 unique stars in RAVE DR6 that have acceptable quality-flags from the MADERA stellar parameter pipeline ([Steinmetz et al. 2020b](#)), photometric metallicity and temperature estimates are taken from the SkyMapper Southern Survey (SMSS; [Wolf et al. 2018](#)) Data Release 2 (DR2; [Onken et al. 2019](#)). These estimates are derived by the procedure described in [Huang et al. \(2021b\)](#) and explained below. Metal-poor candidate stars from RAVE are also taken from the sample in [Placco et al. \(2018\)](#) whose authors explored the nature of the RAVE stellar parameters with a corresponding set of spectroscopic parameters, also explained below.

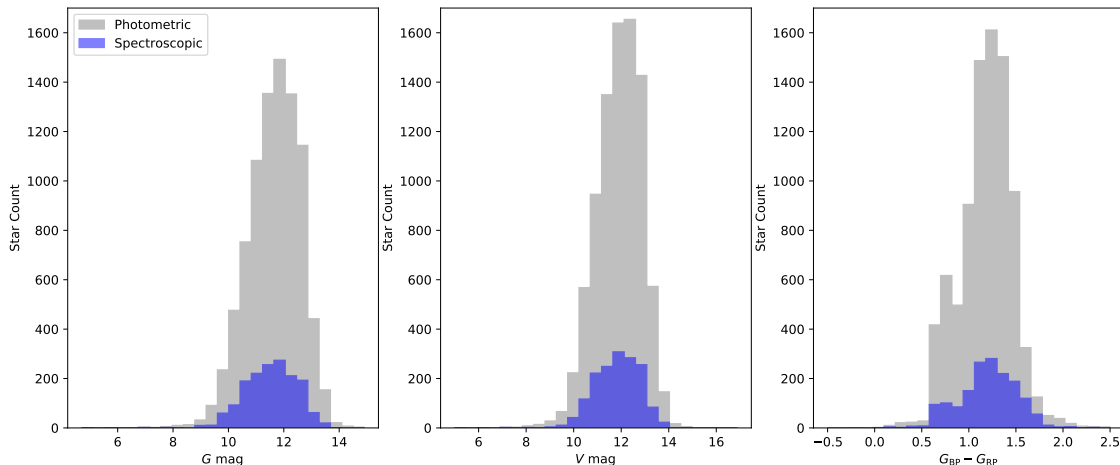


**Figure 2.** Left Panel: Histogram of the  $G_{\text{mag}}$  for the Full Sample. Middle Panel: Histogram of the  $V_{\text{mag}}$  for the Full Sample. Right Panel: Histogram of the  $G_{\text{BP}} - G_{\text{RP}}$  color for the Full Sample. All Panels: The spectroscopic subset of the Full Sample is represented as a blue histogram; the photometric subset is represented as a gray histogram.

The validation spectra from [Placco et al. \(2018\)](#)<sup>3</sup> were then used to determine the stellar atmospheric parameters and elemental abundances for the stars using the non-SEGUE Stellar Parameter Pipeline (n-SSPP; [Beers et al. 2014, 2017](#)), following the procedures described in Paper I. The parameters obtained are the effective temperature ( $T_{\text{eff, Spec}}$ ), surface gravity ( $\log g$ ), and metallicity ( $[\text{Fe}/\text{H}]_{\text{Spec}}$ ), while the elemental abundances are the carbon abundance ( $[\text{C}/\text{Fe}]$ ), and the  $\alpha$ -element abundance ( $[\alpha/\text{Fe}]$ ). The carbon abundance is then adjusted, using the prescription outlined in [Placco et al. \(2014\)](#), to account for the depletion of carbon along the red giant branch. This corrected carbon abundance ( $[\text{C}/\text{Fe}]_c$ ) is used as the star’s natal carbon abundance. The average errors adopted for each of the stellar parameters for the spectra with  $\text{S/N} \sim 30$  are  $\pm 150$  K for  $T_{\text{eff}}$ ;  $\pm 0.35$  dex for  $\log g$ , and  $\pm 0.20$  dex for  $[\text{Fe}/\text{H}]$ ,  $[\text{C}/\text{Fe}]$ , and  $[\alpha/\text{Fe}]$ , with values for each star listed in Table 8 in the Appendix (See [Lee et al. 2008](#) for more information on the errors). Note that the elemental abundances reported here supersede those published in [Placco et al. \(2018\)](#)<sup>4</sup>.

<sup>3</sup> A comprehensive explanation of the construction of the spectroscopic sample, along with details of the medium-resolution spectroscopic observations, are discussed in [Placco et al. \(2018\)](#) and Paper I, to which we refer the interested reader.

<sup>4</sup> The  $[\text{C}/\text{Fe}]$  and  $\alpha$ -element abundances present in [Placco et al. \(2018\)](#) were found to be systematically offset; the updated values are listed here. The stellar parameters were not affected, in general, although there are occasionally different reported  $[\text{Fe}/\text{H}]_{\text{Spec}}$  values reported based on later re-inspections of the spectra by Beers.

The rest of our sample is assembled from recent photometric estimates of temperature, luminosity classes, and metallicity for candidate stars from the RAVE DR6 survey based on the procedure described by [Huang et al. \(2021b\)](#). This study made use of recalibrated zero-points ([Huang et al. 2021a](#)) in the narrow- and medium-band photometry obtained by the Sky Mapper Southern Survey (SMSS; [Wolf et al. 2018](#)) Data Release 2 (DR2; [Onken et al. 2019](#)), along with broad-band photometry from Gaia EDR3 ([Gaia Collaboration et al. 2021](#)). The average errors adopted for each of the stellar parameters for the photometric portion of the sample are  $\pm 62$  K for  $T_{\text{eff}}$ , and  $\pm 0.13$  dex for  $[\text{Fe}/\text{H}]$ , with values for each star listed in Table 8 in the Appendix (See [Huang et al. 2021b](#) for more information on the errors). [Huang et al. \(2021b\)](#) have compared the photometric estimates of  $T_{\text{eff}}$  and  $[\text{Fe}/\text{H}]$  from their catalog with several medium-resolution studies (including stars from the Pristine Survey follow-up reported by [Aguado et al. 2019](#), and from the Best & Brightest sample reported by [Limberg et al. 2021b](#)) and high-resolution studies that employed near-IR spectroscopy from APOGEE DR14 ([Abolfathi et al. 2018](#)) and DR16 ([Ahumada et al. 2020](#)), as well as optical high-resolution spectroscopy from a number of individual papers, and find generally excellent agreement. A total of 8205 stars have available photometric estimates of effective temperature and metallicity within desired ranges ( $[\text{Fe}/\text{H}]_{\text{Phot}} \leq -0.8$  and  $4250 \leq T_{\text{eff, Phot}} \text{ (K)} \leq 7000$ ); 1303 of these stars also have available medium-resolution spectra. The total number of stars available is 8675, when duplicates are properly taken in considera-

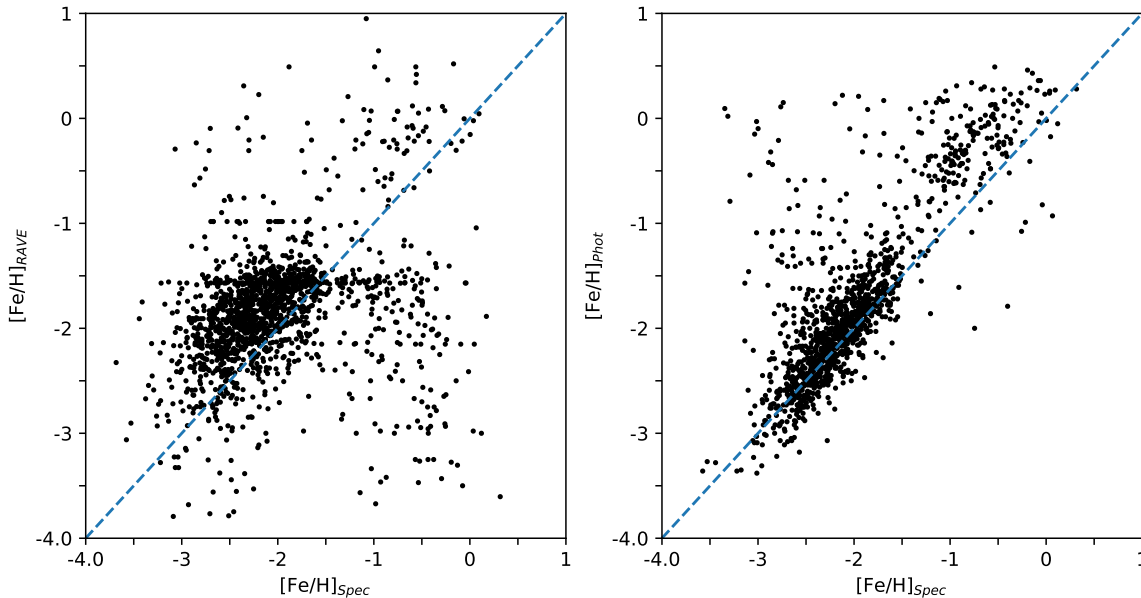


**Figure 3.** Left: Comparison plot between the spectroscopic metallicity from the n-SSPP ( $[\text{Fe}/\text{H}]_{\text{Spec}}$ ) and the RAVE DR6 metallicity ( $[\text{Fe}/\text{H}]_{\text{RAVE}}$ ) in the Full Sample. Right: Comparison plot between the spectroscopic metallicity from the n-SSPP ( $[\text{Fe}/\text{H}]_{\text{Spec}}$ ) and the photometric metallicity estimates from Huang et al. (2021b) ( $[\text{Fe}/\text{H}]_{\text{Phot}}$ ) in the Full Sample.

tion between the spectroscopic and photometric sources through the process discussed in the next section.

We refer to these stars as the Full Sample. The spatial distribution of the Full Sample in Galactic coordinates can be seen in Figure 1. Figure 2 compares the distributions of apparent magnitudes and colors for the Full Sample stars, as described in more detail below. Trimming of this sample to obtain a subset of stars suitable for our dynamical analysis is described below for the Initial Sample.

## 2.2. Construction of the Initial Sample

The metallicities from both RAVE DR6 and SMSS DR2 photometric estimates were available to construct the Initial Sample. Here we explore the comparison between the two metallicity sets and provide reasoning on our selection methods.

### 2.2.1. Comparing RAVE DR6 and Photometric Metallicities

Comparisons of the metallicity estimates of the RAVE values to those with updated spectroscopic stellar parameters revealed a significant dispersion among the RAVE measurements, as can be appreciated in the left panel of Figure 3. The comparison between the photometric estimates of the metallicity and the spectroscopic metallicity is shown in the same figure in the right panel. The biweight (see Beers et al. 1990) estimates of offsets and scale in the residuals between the RAVE

DR6 metallicities and the spectroscopic metallicities (in the sense  $[\text{Fe}/\text{H}]_{\text{RAVE}} - [\text{Fe}/\text{H}]_{\text{Spec}}$ ) is  $\mu = +0.32$  dex and  $\sigma = 0.57$  dex, respectively, while the biweight offset and scale in the residuals between the photometric metallicities and spectroscopic metallicities (in the sense  $[\text{Fe}/\text{H}]_{\text{Phot}} - [\text{Fe}/\text{H}]_{\text{Spec}}$ ) determined from the validation spectra is  $\mu = +0.12$  dex and  $\sigma = 0.30$  dex, respectively. Based on these behaviors, we decided to use the photometric determinations based on the recalibrated SMSS DR2 from Huang et al. (2021b) for the present analysis, rather than the RAVE DR6 estimates.

### 2.2.2. Comparing Spectroscopic and Photometric Parameters

The comparison between metallicity determinations from both the spectroscopic and photometric estimates can be appreciated in Figure 4. The biweight estimators of location and scale for the metallicity residuals determined from the medium-resolution spectra and the photometric metallicity yield  $\mu = +0.12$  dex and  $\sigma = 0.30$  dex. As noted by Huang et al. (2021b), stars that have enhanced carbon often estimated photometric metallicities that are somewhat higher than the spectroscopic determinations, due to molecular carbon features affecting the blue narrow/medium-band filters  $v$  and  $u$  from SMSS (particularly for cooler carbon-enhanced stars). Stars with  $[\text{C}/\text{Fe}]_c > +0.7$ , which we define as carbon-enhanced metal-poor (CEMP) stars are indicated with red circles around the dots shown in the bottom panel

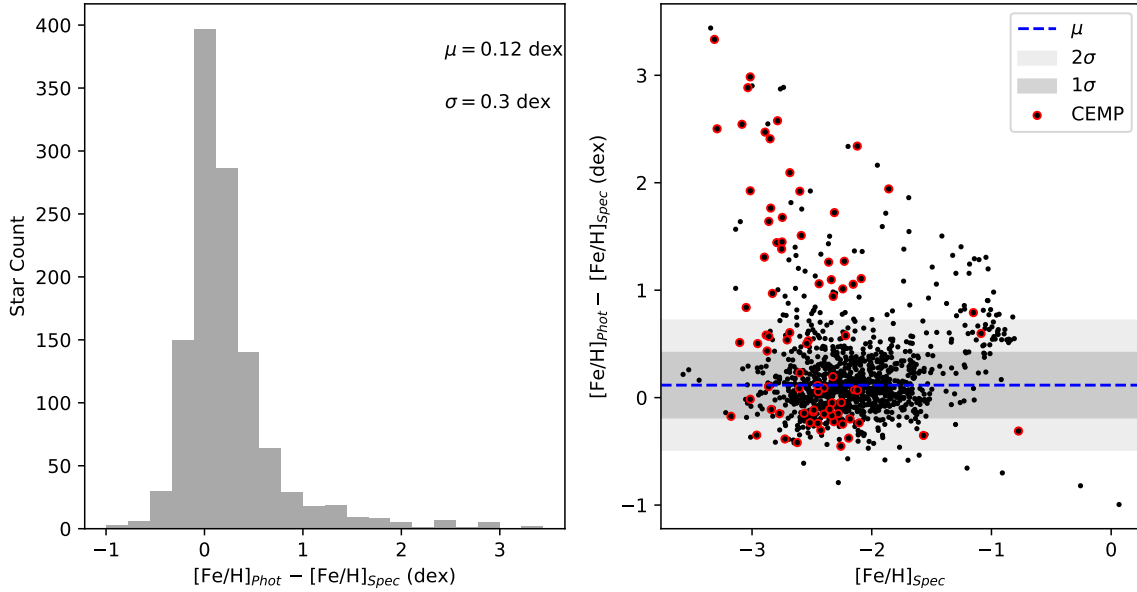


**Figure 4.** Left Panel: Histogram of the residuals of the difference between the photometric metallicity values ( $[\text{Fe}/\text{H}]_{\text{Phot}}$ ) and the metallicity values obtained from medium-resolution spectra ( $[\text{Fe}/\text{H}]_{\text{Spec}}$ ) for the Full Sample. The biweight locations and scales are noted. Right panel: The residuals between  $[\text{Fe}/\text{H}]_{\text{Phot}}$  and  $[\text{Fe}/\text{H}]_{\text{Spec}}$ , as a function of  $[\text{Fe}/\text{H}]_{\text{Spec}}$ , for the Full Sample. CEMP stars are indicated with red outlined points. The blue dashed line is the biweight location, while the shaded regions represent the first ( $1\sigma$ ) and second ( $2\sigma$ ) biweight scale ranges. The apparent systematic discrepancy at high metallicity in this panel is likely due to difficulties in the n-SSPP estimates in this range (see text).

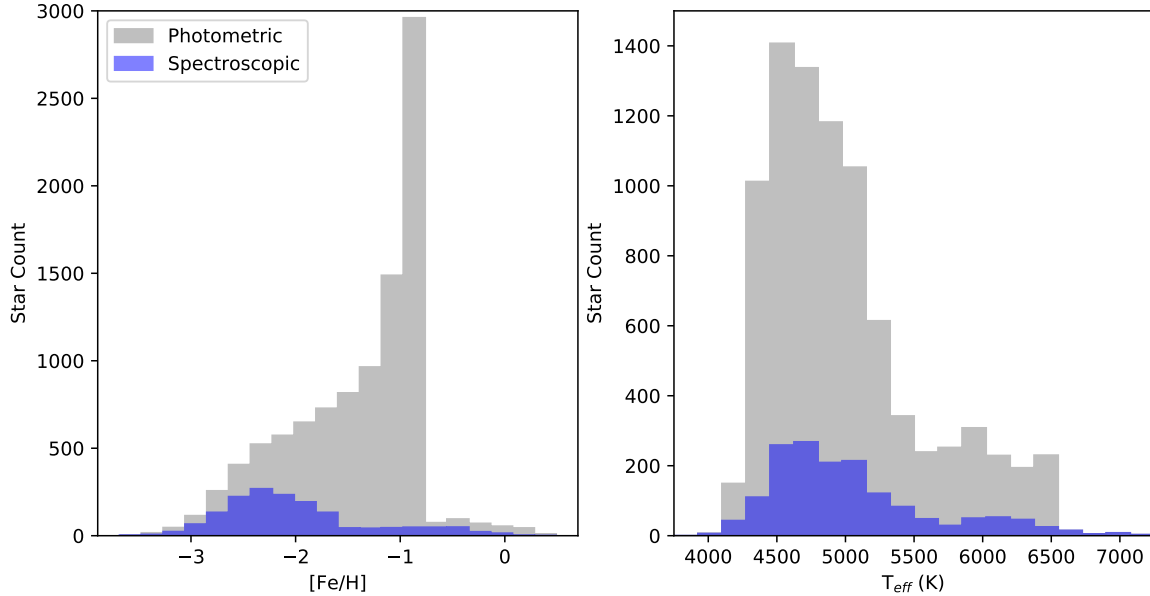


**Figure 5.** Left Panel: Histogram of the metallicity for the spectroscopic ( $[\text{Fe}/\text{H}]_{\text{Spec}}$ , blue) and photometric ( $[\text{Fe}/\text{H}]_{\text{Phot}}$ , gray) stars for the Full Sample. Right Panel: Histogram of the effective temperatures for the spectroscopic ( $T_{\text{eff Spec}}$ , blue) and photometric ( $T_{\text{eff Phot}}$ , gray) stars for the Full Sample. Although the effective temperature distributions for the two subsets appear similar, the spectroscopic sample of stars clearly favors stars with lower  $[\text{Fe}/\text{H}]$ , by design.

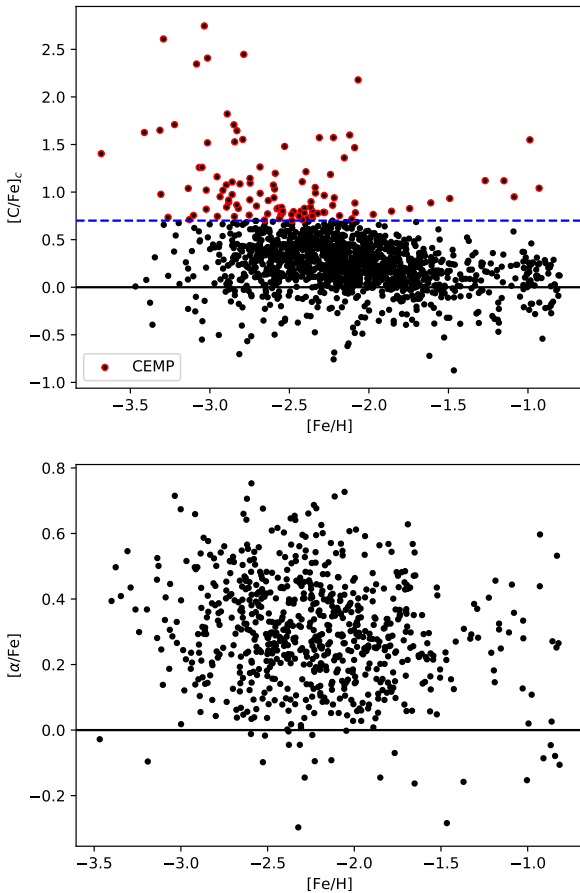


**Figure 6.** Top Panel: The corrected carbon abundance ( $[C/Fe]_c$ ) of the Initial Sample, as a function of the final metallicity ( $[Fe/H]$ ) for stars with  $[Fe/H] \leq -0.8$ . The CEMP cutoff ( $[C/Fe]_c = +0.7$ ) is noted as the blue dashed line; CEMP stars are indicated with red outlined points. The Solar value is indicated as the solid black line. Bottom panel: The  $\alpha$ -element abundance ( $[\alpha/Fe]$ ) of the Initial Sample, as a function of the final metallicity ( $[Fe/H]$ ). The Solar value is indicated with a solid black line.

of Figure 4. We note that, when these stars are removed from the sample, similar offsets and residuals are found as for the entire sample.

From inspection of this figure, there appears to be a systematic discrepancy in the metallicity estimates in the metal-rich region. As in Paper I, we attribute this

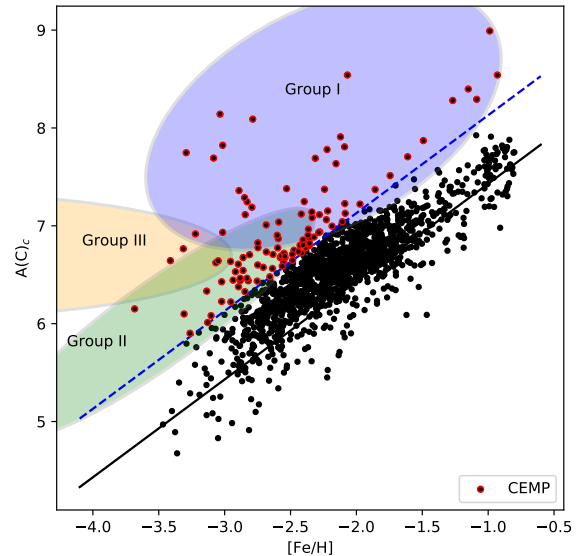


**Figure 7.** The Yoon-Beers Diagram of  $A(C)_c$ , as a function of  $[Fe/H]$ , for stars in the Initial Sample. The CEMP cutoff ( $[C/Fe]_c = +0.7$ ) is indicated with a blue dashed line. The CEMP stars ( $[C/Fe]_c > +0.7$ ) are shown as red outlined points.  $[C/Fe] = 0$  is indicated with a solid black line. The ellipses represent the three different morphological groups of CEMP stars (See Figure 1 in Yoon et al. 2016 for a comparison and more information).

to difficulties encountered by the n-SSPP estimates<sup>5</sup>, rather than the photometric estimates, which have been shown by Huang et al. (2021b) to have excellent performance in this metallicity regime. As noted below, we only retain stars with  $[Fe/H] \leq -0.8$  in the Final Sample, so these stars will not greatly affect our subsequent analysis.

Figure 5 shows the distributions of  $[Fe/H]$  and  $T_{\text{eff}}$  estimates obtained from the photometric and spectroscopic sub-samples. As can be appreciated from inspection of this figure, although these subsets are similarly distributed over  $T_{\text{eff}}$  (right panel), the majority of the the stars in the spectroscopic validation sample have  $[Fe/H] \lesssim -1.8$  (left panel), resulting from the selection of very low-metallicity candidates for the validation process.

For stars that have both spectroscopic and photometric stellar parameters, we perform a procedure to obtain the parameters available to produce final adopted

<sup>5</sup> The n-SSPP uses a subset of the estimators employed by the SSPP, which has been demonstrated previously to work very well in this high-metallicity range.

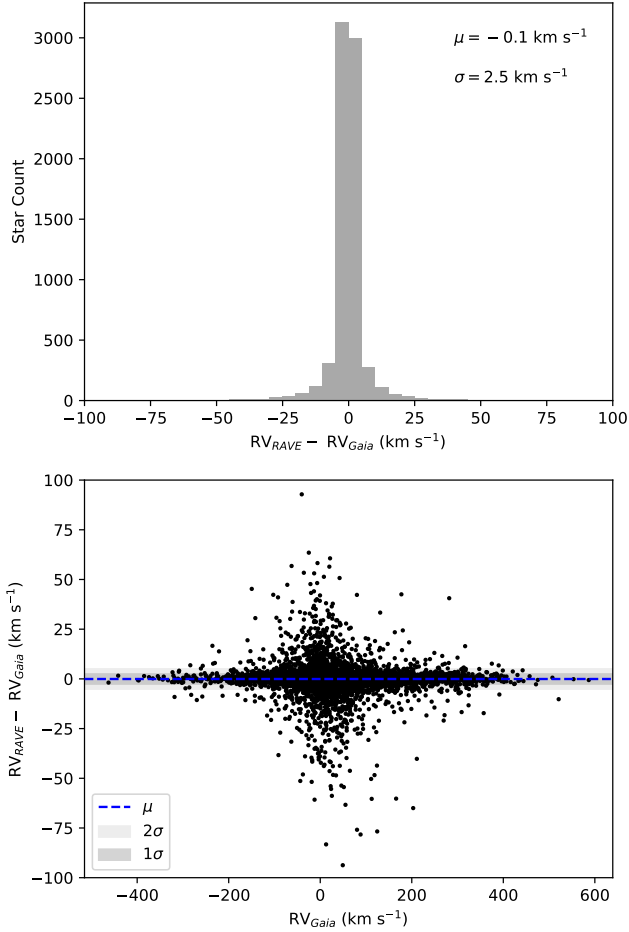


**Figure 8.** Top Panel: Histogram of the residuals of the difference between the RAVE DR6 radial velocities and the Gaia EDR3 values in the Full Sample. The biweight location and scale are noted. Bottom panel: The residuals between the RAVE DR6 and Gaia EDR3 radial velocities in the Full Sample, as a function of the Gaia radial velocities. The blue dashed line is the biweight location of the residual difference ( $\mu = -0.1 \text{ km s}^{-1}$ ), while the shaded regions represent the first ( $1\sigma = 2.5 \text{ km s}^{-1}$ ), and second ( $2\sigma = 5.0 \text{ km s}^{-1}$ ) biweight scale ranges.

estimates of  $[\text{Fe}/\text{H}]$  and  $T_{\text{eff}}$ , as in Paper I. If the absolute difference in metallicity between the two samples ( $[\text{Fe}/\text{H}]_{\text{Spec}} - [\text{Fe}/\text{H}]_{\text{Phot}}$ ) is less than 0.5 dex, then we average the two sets of parameters. If not, then a choice is made to adopt either the spectroscopic or photometric parameters based on visual inspection of the spectrum for a given star. For the stars with available spec-

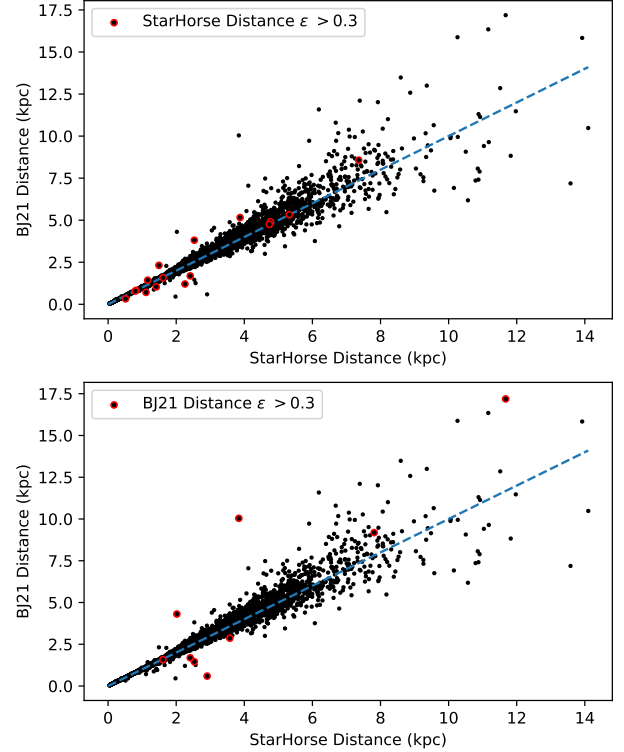


**Figure 9.** Top Panel: Comparison between the StarHorse distances and BJ21 distances in the Full Sample. Stars with the red outlined points indicate that the relative distance error in StarHorse is  $\epsilon > 0.3$ . Bottom panel: The same comparison as the top panel, but with the red outlined points indicating the relative distance error in BJ21 is  $\epsilon > 0.3$ . In both plots the dashed line indicates a one-to-one comparison between the two samples.

troscopy, we then adjust estimates of the carbon and  $\alpha$ -element abundances from the n-SSPP based on the final adopted  $[\text{Fe}/\text{H}]$ .

Restricting stellar values to  $[\text{Fe}/\text{H}] \leq -0.8$  and  $4250 \leq T_{\text{eff}} (\text{K}) \leq 7000$  (consistent with the choices made in Paper I) yields 8377 metal-poor stars for the Initial Sample.

The  $[\text{C}/\text{Fe}]_c$  and  $[\alpha/\text{Fe}]$  estimates for stars in the Initial Sample are shown in Figure 6. The Yoon-Beers diagram of  $A(C)_c$  vs.  $[\text{Fe}/\text{H}]$  for Initial Sample stars is shown in Figure 7. The CEMP stars ( $[\text{C}/\text{Fe}]_c > +0.7$ ) are provided in Table 10 of the Appendix.

The stars from the Full Sample were then cross-matched with Gaia Early Data Release 3 (EDR3; Gaia Collaboration et al. 2021) using a  $5''$  radius to find their 6-D astrometric parameters. To validate the match for each star, confirmation was performed by checking that

the stellar magnitudes agreed to within 0.5 mag between the sources. The Full Sample was mostly taken from  $V$  magnitudes supplied by the AAVSO Photometric All Sky Survey (APASS; Henden & Munari 2014) Data Release 9 (DR9; Henden et al. 2016), with various other sources listed in the Appendix tables supplying the rest. The corresponding matches were then compared with the  $V$  magnitude utilizing the transformation from Gaia magnitudes  $G$ ,  $G_{BP}$ , and  $G_{RP}$  in EDR3 provided in Table C.2 of Riello et al. (2021). A comparison of the magnitudes and colors for the photometric and spectroscopic subsets can be seen in Figure 2. From inspection of the figure, although the relative numbers differ, the distributions are similar to one another.

### 2.3. Construction of the Final Sample

Once stars from the Full Sample are matched with those from Gaia EDR3, dynamical parameters for stars in the Initial Sample can be recovered and used to construct the Final Sample.

#### 2.3.1. Radial Velocities, Distances, and Proper Motions

Radial velocities, parallaxes, and proper motions for each star are taken from Gaia EDR3, when available. Note that the radial velocities for the stars in Gaia EDR3 are available for about 87% of the Full Sample. Typical errors for Gaia EDR3 radial velocities are  $\sim 1$  km s $^{-1}$ . The top panel of Figure 8 shows a histogram of the residual differences between the RAVE DR6 radial velocities and the Gaia EDR3 values. The biweight location and scale of these differences are  $\mu = -0.1$  km s $^{-1}$  and  $\sigma = 2.5$  km s $^{-1}$ , respectively. The bottom panel of this figure shows the residuals between the RAVE DR6 and Gaia EDR3 radial velocities, as a function of the Gaia radial velocities. The blue dashed line is the biweight location, while the shaded regions represent the first ( $1\sigma$ ) and second ( $2\sigma$ ) biweight scale ranges. We expect that many of the stars with residuals outside the  $2\sigma$  range are binaries, causing an improper measurement of the systemic radial velocities.

The distances to the stars are determined either through the StarHorse distance estimate (Anders et al. 2021) or the Bailer-Jones distance estimate (BJ21; Bailer-Jones et al. 2021). Parallax values in our Full Sample from EDR3 have an average error of around 0.04 mas. The StarHorse and BJ21 distances are determined by a Bayesian approach utilizing the EDR3 parallax, magnitude, and color (Anders et al. 2021; Bailer-Jones et al. 2021). The errors are presented for each star in the tables provided in the Appendix. We prioritize the StarHorse distances when the relative error (the error divided by the reported value),  $\epsilon$ , is  $\epsilon < 30\%$ . If the StarHorse relative error is  $\geq 30\%$ , then we adopt the

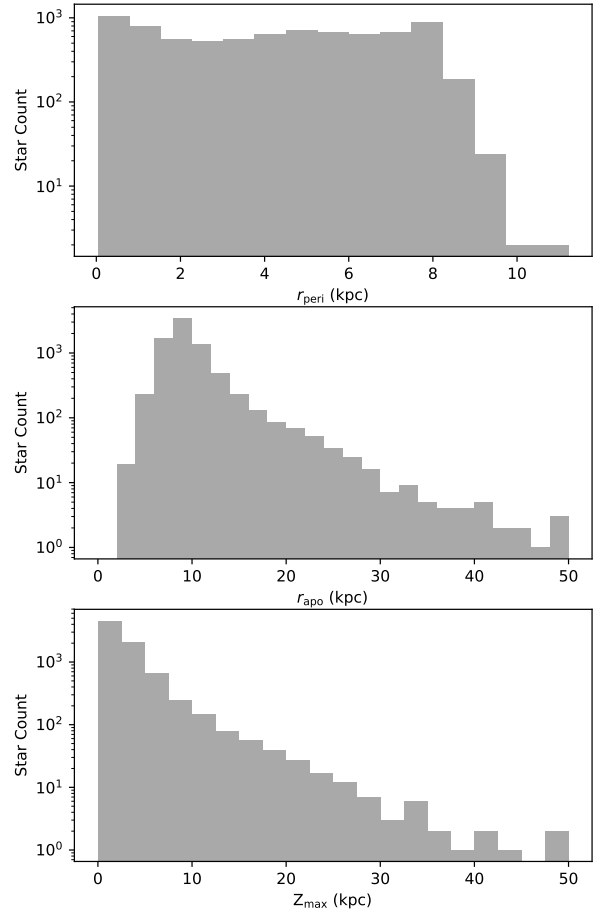


**Figure 10.** Logarithmic histograms of the orbital parameters  $r_{\text{peri}}$  (top),  $r_{\text{apo}}$  (middle), and  $Z_{\text{max}}$  (bottom) for the RAVE DR6 Final Sample. Note that a few stars have  $r_{\text{apo}}$  and  $Z_{\text{max}}$  outside the range shown in the panels.

BJ21 distance if the relative error is  $\epsilon < 30\%$ . If only one distance estimator is available, then we adopt it. If both distances, or the only available distance, have  $\epsilon \geq 30\%$ , then we discard the star from the dynamical analysis below. Note that in Figure 9 the StarHorse and BJ21 approaches produce similar distances, especially when the distance is smaller than 5 kpc. A comparison between Figure 9 and Figure 8 in Paper I clearly shows the improvement in the distance estimators when the StarHorse distances are used in comparison to the Gaia EDR3 inverse-parallax distances employed in Paper I. The proper motions in our Full Sample from Gaia EDR3 have an average error of  $39 \mu\text{s yr}^{-1}$ .

### 2.4. Dynamical Parameters

The orbital characteristics of the stars are determined using the Action-based GALaxy Modelling Architecture<sup>6</sup> (AGAMA) package (Vasiliev 2019), using the same Solar positions and peculiar motions described in Paper I<sup>7</sup>. The MW gravitational potential we adopt is the MW2017 potential (McMillan 2017), also described in Paper I. The 6D astrometric parameters, determined in Section 2, are run through the orbital integration process in AGAMA using the same procedure outlined in Paper I to calculate the orbital energy, cylindrical positions and velocities, angular momentum, cylindrical actions, and eccentricity. See Paper I for definitions of these orbital parameters.

The above procedure obtains the orbital parameters if the astrometric parameters are precisely described by the given values. However, these values have errors associated with them, so a method must be developed to estimate the errors in the orbital parameters. This is accomplished through a Monte Carlo sampling over the errors in the astrometric parameters. The procedure that we employ to determine the orbital errors using Monte Carlo sampling is described in detail in Paper I.

An inspection is performed to identify stars that are not suitable for the following dynamical analysis. The Initial Sample of 8377 stars contains stars that are unbound from the MW ( $E > 0$ ), along with stars that do not have the full 6-D astrometric parameters of position, radial velocity, distance, and proper motions were then cut. Finally, in order to obtain accurate orbital dynamics, we remove 401 stars with differences in their RAVE DR6 radial velocities compared to the Gaia radial velocities that lie outside the  $15 \text{ km s}^{-1}$  range. Most of these stars are expected to be binaries. Application of this cut leaves a total sample of 7957 stars to perform the following analysis. The dynamical parameters of the stars with orbits determined are listed in Table 9 in the Appendix; we refer to this as the Final Sample.

Figure 10 provides histograms of  $r_{\text{apo}}$  (top),  $r_{\text{peri}}$  (middle), and  $Z_{\text{max}}$  (bottom) for the Final Sample. From inspection of this figure, it is clear that the majority of the stars in this sample occupy orbits that take them inside the inner-halo region, but they also explore

regions well into the outer-halo region, up to  $\sim 50 \text{ kpc}$  away.

### 3. CLUSTERING PROCEDURE

Helmi & de Zeeuw (2000) were among the first to suggest the use of integrals of motion, in their case orbital energy and angular momenta, to find substructure in the MW using the precision measurements of next-generation surveys that were planned at the time. McMillan & Binney (2008) suggested the use of actions as a complement to the previously suggested orbital energy and angular momenta, with only the vertical angular momentum being invariant in an axisymmetric potential. Most recently, many authors have employed the orbital energy and cylindrical actions ( $E, J_r, J_\phi, J_z$ ) to determine the substructure of the MW using Gaia measurements (Helmi et al. 2017; Myeong et al. 2018a,b; Roederer et al. 2018; Naidu et al. 2020; Yuan et al. 2020b,a; Gudín et al. 2021; Limberg et al. 2021a; Shank et al. 2021).

As described in Paper I, we employ HDBSCAN in order to perform a cluster analysis over the orbital energy and cylindrical actions from the Final Sample obtained through the procedure outlined in Section 2.3. The HDBSCAN algorithm<sup>8</sup> operates through a series of calculations that are able to separate the background noise from denser clumps of data in the dynamical parameters. We utilize the following parameters described in Paper I: `~min_cluster_size = 5`, `~min_samples = 5`, `~cluster_selection_method = 'leaf'`, `~prediction_data = ~True`, Monte Carlo samples at 1000, and minimum confidence set to 20%.

Table 1 provides a listing of the Dynamically Tagged Groups (DTGs) identified by this procedure, along with their numbers of member stars, confidence values, and associations described below. Note that, although a minimum confidence value of 20% was employed, the actual minimum value found for these DTGs is 23.9%. The DTGs and CDTGs are identified using the nomenclature introduced by Yuan et al. (2020a), to which we refer the interested reader.

Table 2 lists the stellar members of the identified DTGs, along with their final values of  $[\text{Fe}/\text{H}]$ ,  $[\text{C}/\text{Fe}]$ ,  $[\text{C}/\text{Fe}]_c$ , and  $[\alpha/\text{Fe}]$ , where available. The last line in the listing for each DTG gives the mean and dispersion (both using biweight estimates) for each quantity.

Table 3 lists the identified DTGs where at least half of the member stars have  $[\text{C}/\text{Fe}]$  and  $[\alpha/\text{Fe}]$  detected.

<sup>6</sup> <http://github.com/GalacticDynamics-Oxford/Agama>

<sup>7</sup> We adopt a Solar position of  $(-8.249, 0.0, 0.0) \text{ kpc}$  (Gravity Collaboration et al. 2020) and Solar peculiar motion in  $(U, W)$  as  $(11.1, 7.25) \text{ km s}^{-1}$  (Schönrich et al. 2010) with Galactocentric Solar azimuthal velocity  $V = 250.70 \text{ km s}^{-1}$  determined from Reid & Brunthaler (2020).

<sup>8</sup> For a detailed description of the HDBSCAN algorithm visit: [https://hdbscan.readthedocs.io/en/latest/how\\_hdbscan\\_works.html](https://hdbscan.readthedocs.io/en/latest/how_hdbscan_works.html)

**Table 1.** Identified DTGs

DTG	<i>N</i> Stars	Confidence	Associations
1	35	99.0%	new
2	30	79.0%	DS21:DTG-13
3	30	93.0%	new
4	28	90.5%	DS21:DTG-4, DG21:CDTG-18, GM18a:C1, HL19:GL-2, GL21:DTG-8
5	27	77.1%	Splashed Disk
6	24	59.1%	DS21:DTG-47
7	23	87.7%	GSE, IR18:E, DG21:CDTG-1, EV21:NGC 4833, GC21:Sausage, GL21:DTG-37, DS21:DTG-43
8	23	95.5%	GSE, DS21:DTG-3, GC21:Sausage, DG21:CDTG-9, GL21:DTG-34
9	23	86.4%	new
10	22	98.9%	DS21:DTG-12

NOTE—We adopt the nomenclature for previously identified DTGs and CDTGs from Yuan et al. (2020a).

NOTE—This table is a stub; the full table is available in the electronic edition.

Table 4 lists the derived dynamical parameters derived by AGAMA used in our analysis.

#### 4. STRUCTURE ASSOCIATIONS

Associations between the newly identified DTGs are now sought between known MW structures, including large-scale substructures, previously identified dynamical groups, stellar associations, globular clusters, and dwarf galaxies.

##### 4.1. Milky Way Substructures

Analyzing the orbital energy and actions is not sufficient to determine separate large-scale substructures. Information on the elemental abundances is crucial due to the differing star-formation histories of the structures, which can vary in both mass and formation redshift (Naidu et al. 2020). The outline for the prescription used to determine the structural associations with our DTGs is described in Naidu et al. (2020), and explained in detail in Paper I. Simple selections are performed based on physically motivated choices for each substructure, excluding previously defined substructures, as the process iterates to decrease contamination between substructures. Following their procedures, we find 6 predominant MW substructures associated with our DTGs, listed in Table 5. This table provides the numbers of stars in each substructure, the mean and dispersion of their chemical abundances, and the mean and dispersion of their dynamical parameters for each substructure. The Lindblad diagram and projected-action plot for these substructures is shown in Figure 11.

##### 4.1.1. Gaia-Sausage-Enceladus

The most populated substructure is Gaia-Sausage-Enceladus (GSE), which contains 523 member stars. GSE is thought to be a remnant of an earlier merger that distributed a significant number of stars throughout the inner halo of the MW (Belokurov et al. 2018; Helmi et al. 2018). The action space determined by the member stars exhibits an extended radial component, a null azimuthal component within errors, and a null vertical component. These orbital properties are the product of the high-eccentricity selection of the DTGs, and agree with previous findings of GSE orbital characteristics when using other selection criteria (Koppelman et al. 2018; Myeong et al. 2018a; Limberg et al. 2021a).

The  $\langle[\text{Fe}/\text{H}]\rangle$  of GSE found in our work is rather metal poor ( $[\text{Fe}/\text{H}] \sim -1.5$ ), consistent with studies of its metallicity in dynamical groupings, even though our sample contains more metal-rich stars that could have been associated with GSE (Gudin et al. 2021; Limberg et al. 2021a). The stars that form DTGs in GSE tend to favor the more metal-poor tail of the substructure, which is also seen in previous DTG analysis. The  $\langle[\alpha/\text{Fe}]\rangle$  of GSE exhibits a relatively low level, consistent with the low-Mg structure detected by Hayes et al. (2018) and with Mg levels consistent with accreted structures simulated by Mackereth et al. (2019). The  $\alpha$ -element enhancement seen in GSE is due to accretion of older stellar populations, consistent with known element abundance patterns. We also obtain a  $\langle[\text{C}/\text{Fe}]_c\rangle$  for GSE (note that stars from Huang et al. 2021b do not have measurements of  $[\text{C}/\text{Fe}]_c$  or  $[\alpha/\text{Fe}]$ ). Finally, we can associate the globular clusters Ryu 879 (RLGC2), IC

**Table 2.** DTGs Identified by HDBSCAN

RAVE ID	[Fe/H]	[C/Fe]	[C/Fe] <sub>c</sub>	[ $\alpha$ /Fe]
<i>DTG – 1</i>				
Structure: Unassigned Structure				
Group Assoc: No Group Associations				
Stellar Assoc: No Stellar Associations				
Globular Assoc: No Globular Associations				
Dwarf Galaxy Assoc: No Dwarf Galaxy Associations				
J124828.60–463558.7	–0.910	...	...	...
J134259.33–420116.0	–0.970	...	...	...
J145237.82–394929.1	–0.860	...	...	...
J145301.90–734037.1	–1.390	...	...	...
J145314.34–255954.2	–0.860	...	...	...
J145848.84–380905.7	–1.000	...	...	...
J153735.89–025256.1	–0.840	...	...	...
J160708.39–025922.7	–0.970	...	...	...
J161555.25–004906.2	–1.200	...	...	...
J161821.47–023635.3	–0.820	...	...	...
J162133.93–075800.0	–1.090	...	...	...
J162608.99–062248.1	–1.080	...	...	...
J182742.83–513704.2	–2.170	...	...	...
J184219.23–754942.7	–0.920	...	...	...
J190528.57–384355.5	–2.310	...	...	...
J191626.47–630945.4	–0.900	...	...	...
J191718.05–422357.3	–0.880	...	...	...
J191738.19–602128.7	–0.900	...	...	...
J195053.84–401254.9	–1.570	...	...	...
J195603.92–534035.6	–0.800	...	...	...
J195610.10–452825.4	–1.080	...	...	...
J195924.29–282505.1	–0.920	...	...	...
J200012.26–582218.7	–0.940	...	...	...
J200344.00–274647.1	–0.870	...	...	...
J202109.85–153156.4	–0.920	...	...	...
J202128.83–392854.3	–1.180	...	...	...
J203015.48–353149.9	–0.900	...	...	...
J203540.97–082246.7	–0.950	...	...	...
J204434.37–144211.0	–0.810	...	...	...
J205829.82–181249.9	–1.660	...	...	...
J210531.08–025632.7	–1.280	...	...	...
J210711.66–160721.0	–0.840	...	...	...
J213042.25–151010.3	–0.810	...	...	...
J215617.20–180737.8	–0.890	...	...	...
J220930.99–261800.8	–0.880	...	...	...
$\mu \pm \sigma$ ([X/Y])	$-0.921 \pm 0.132$	...	...	...

NOTE— $\mu$  and  $\sigma$  represent the biweight estimates of the location and scale for the abundances in the DTG.

NOTE—This table is a stub; the full table is available in the electronic edition.

1257, NGC 4833, NGC 5139 ( $\omega$ Cen), and NGC 6284 with GSE, based on DTGs with similar orbital characteristics of these globular clusters (see Sec. 4.3 for details). Note in Figure 11 how GSE occupies a large region of the Lindblad diagram, concentrated in the planar and radial portions of the projected-action plot.

#### 4.1.2. The Metal-Weak Thick Disk

The second-most populated substructure is the Metal-Weak Thick Disk (MWTD), which contains 119 member stars. The MWTD is thought to have formed from either a merger scenario, possibly related to GSE, or the result of old stars born within the Solar radius migrating out to the Solar position due to tidal instabilities within the MW (Carollo et al. 2019). The non-existent radial and vertical velocity components, as well as the large posi-

**Table 3.** DTGs Identified by HDBSCAN with Carbon and  $\alpha$ -Elements

	[Fe/H]	[C/Fe]	[C/Fe] <sub>c</sub>	[ $\alpha$ /Fe]
<i>DTG – 4</i> [ $N_C$ : (14/28) and $N_\alpha$ : (11/28)]				
Structure: Unassigned Structure				
Group Assoc: C1: <a href="#">Myeong et al. (2018a)</a>				
Group Assoc: GL-2: <a href="#">Li et al. (2019)</a>				
Group Assoc: DTG-8: <a href="#">Limberg et al. (2021a)</a>				
Group Assoc: DTG-4: <a href="#">Shank et al. (2021)</a>				
Stellar Assoc: J113738.01-520224.8 (DTG-4: <a href="#">Shank et al. (2021)</a> )				
Stellar Assoc: 2MASS J15075699-0659593 (CDTG-18: <a href="#">Gudin et al. (2021)</a> )				
Stellar Assoc: J225118.77-381438.6 (DTG-4: <a href="#">Shank et al. (2021)</a> )				
Stellar Assoc: 2MASS J23362202-5607498* (CDTG-18: <a href="#">Gudin et al. (2021)</a> )				
Globular Assoc: No Globular Associations				
Dwarf Galaxy Assoc: No Dwarf Galaxy Associations				
$\mu \pm \sigma$ ([X/Y])	$-2.074 \pm 0.595$	$-0.284 \pm 0.451$	$+0.357 \pm 0.286$	$+0.351 \pm 0.157$
<i>DTG – 47</i> [ $N_C$ : (5/11) and $N_\alpha$ : (5/11)]				
Structure: Thamnos				
Group Assoc: Sequoia: <a href="#">Cordoni et al. (2021)</a>				
Stellar Assoc: TYC 8420-259-1 (VelHel-4: <a href="#">Helmi et al. (2017)</a> )				
Globular Assoc: No Globular Associations				
Dwarf Galaxy Assoc: No Dwarf Galaxy Associations				
$\mu \pm \sigma$ ([X/Y])	$-1.829 \pm 0.592$	$-0.038 \pm 0.567$	$+0.269 \pm 0.165$	$+0.434 \pm 0.224$
<i>DTG – 67</i> [ $N_C$ : (8/10) and $N_\alpha$ : (8/10)]				
Structure: LMS-1 (Wukong)				
Group Assoc: Comoving: <a href="#">Myeong et al. (2017)</a>				
Group Assoc: C1: <a href="#">Myeong et al. (2018a)</a>				
Group Assoc: Cand11: <a href="#">Myeong et al. (2018b)</a>				
Group Assoc: CDTG-4: <a href="#">Gudin et al. (2021)</a>				
Group Assoc: DTG-2: <a href="#">Limberg et al. (2021a)</a>				
Stellar Assoc: 2MASS J00182832-3900338 (CDTG-4: <a href="#">Gudin et al. (2021)</a> )				
Stellar Assoc: 2MASS J00413026-4058547 (CDTG-4: <a href="#">Gudin et al. (2021)</a> )				
Stellar Assoc: 2MASS J00453930-7457294 (CDTG-4: <a href="#">Gudin et al. (2021)</a> )				
Globular Assoc: No Globular Associations				
Dwarf Galaxy Assoc: No Dwarf Galaxy Associations				
$\mu \pm \sigma$ ([X/Y])	$-2.386 \pm 0.404$	$-0.177 \pm 0.537$	$+0.263 \pm 0.317$	$+0.379 \pm 0.170$
<i>DTG – 71</i> [ $N_C$ : (5/9) and $N_\alpha$ : (4/9)]				
Structure: Gaia-Sausage-Enceladus (GSE)				
Group Assoc: DTG-37: <a href="#">Limberg et al. (2021a)</a>				
Stellar Assoc: TYC 5830-840-1 (VelHel-6: <a href="#">Helmi et al. (2017)</a> )				
Globular Assoc: No Globular Associations				
Dwarf Galaxy Assoc: No Dwarf Galaxy Associations				
$\mu \pm \sigma$ ([X/Y])	$-1.780 \pm 0.362$	$-0.074 \pm 0.237$	$+0.253 \pm 0.005$	$+0.320 \pm 0.140$
<i>DTG – 78</i> [ $N_C$ : (6/9) and $N_\alpha$ : (4/9)]				
Structure: Gaia-Sausage-Enceladus (GSE)				
Group Assoc: CDTG-14: <a href="#">Gudin et al. (2021)</a>				
Stellar Assoc: 2MASS J00541965-0611555* (CDTG-14: <a href="#">Gudin et al. (2021)</a> )				
Stellar Assoc: 2MASS J08155667-2204105 (CDTG-14: <a href="#">Gudin et al. (2021)</a> )				
Stellar Assoc: 2MASS J10044858-2706500* (CDTG-14: <a href="#">Gudin et al. (2021)</a> )				
Globular Assoc: No Globular Associations				
Dwarf Galaxy Assoc: No Dwarf Galaxy Associations				
$\mu \pm \sigma$ ([X/Y])	$-2.222 \pm 0.349$	$+0.004 \pm 0.365$	$+0.519 \pm 0.154$	$+0.392 \pm 0.221$

NOTE—This table lists the DTGs where around half of the member stars have both [C/Fe] and [ $\alpha$ /Fe] detected.  $N_C$  ( $N_\alpha$ ) indicates the total number of Carbon ( $\alpha$ ) detections in comparison to the total number of stars in the DTG.

NOTE— $\mu$  and  $\sigma$  represent the biweight estimates of the location and scale for the abundances in the DTG.

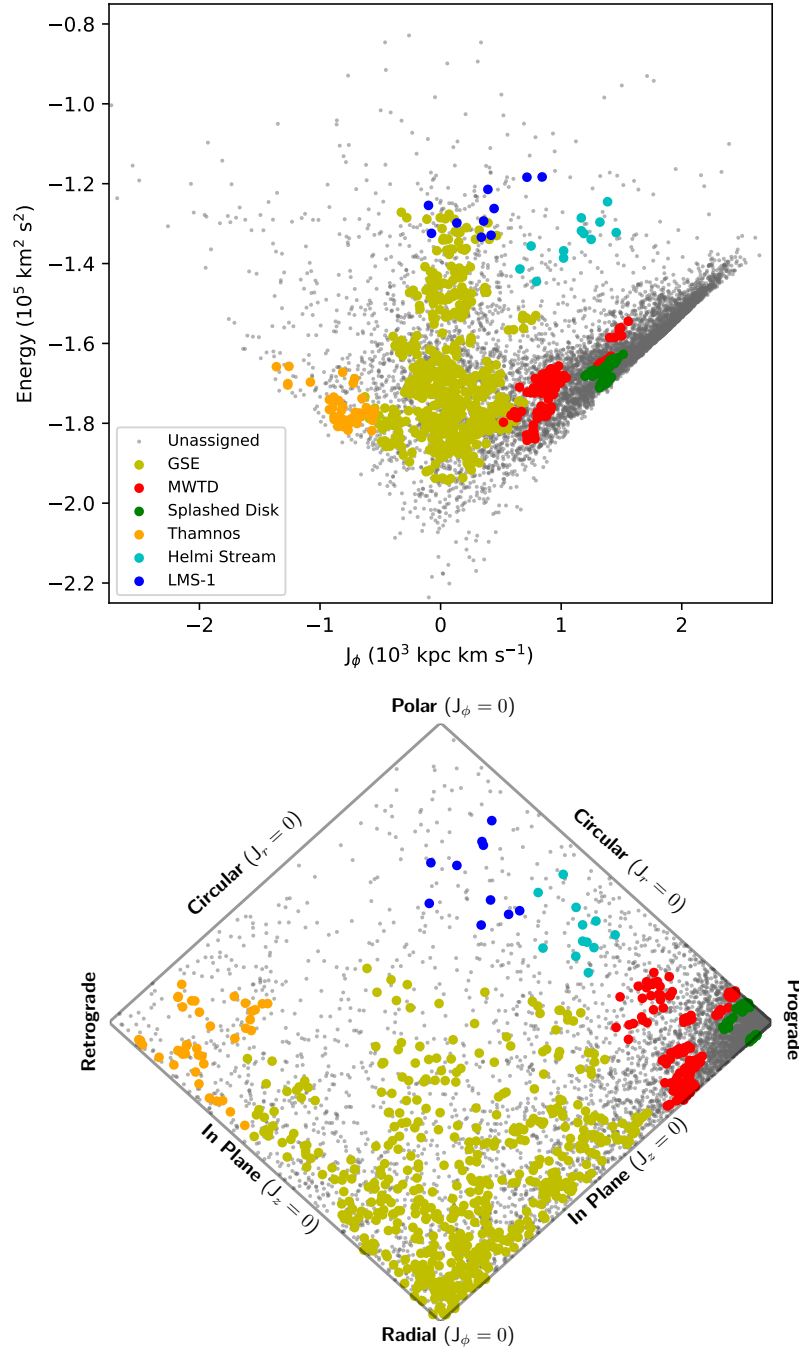


**Figure 11.** Top Panel: Lindblad Diagram of the identified MW substructures. The different structures are associated with the colors outlined in the legend. Bottom Panel: The projected-action plot of the same substructures. This space is represented by  $J_\phi/J_{\text{Tot}}$  for the horizontal axis and  $(J_z - J_r)/J_{\text{Tot}}$  for the vertical axis with  $J_{\text{Tot}} = J_r + |J_\phi| + J_z$ . For more details on the projected-action space, see Figure 3.25 in Binney & Tremaine (2008).

**Table 4.** Cluster Dynamical Parameters Determined by AGAMA

Cluster	N Stars	$(\langle v_r \rangle, \langle v_\phi \rangle, \langle v_z \rangle)$	$(\langle J_r \rangle, \langle J_\phi \rangle, \langle J_z \rangle)$	$\langle E \rangle$	$\langle ecc \rangle$
		$(\sigma_{\langle v_r \rangle}, \sigma_{\langle v_\phi \rangle}, \sigma_{\langle v_z \rangle})$	$(\sigma_{\langle J_r \rangle}, \sigma_{\langle J_\phi \rangle}, \sigma_{\langle J_z \rangle})$	$\sigma_{\langle E \rangle}$	$\sigma_{\langle ecc \rangle}$
		(km s <sup>-1</sup> )	(kpc km s <sup>-1</sup> )	(10 <sup>5</sup> km <sup>2</sup> s <sup>-2</sup> )	
<i>DTG - 1</i>	35	(12.9,133.3,7.6) (59.1,9.8,39.8)	(140.5,899.3,44.5) (23.8,44.2,10.4)	-1.810 0.018	0.419 0.034
<i>DTG - 2</i>	30	(-8.7,259.0,0.7) (19.5,2.8,15.7)	(23.8,2116.6,2.6) (4.8,14.5,2.1)	-1.496 0.003	0.126 0.012
<i>DTG - 3</i>	30	(13.1,183.3,-3.7) (41.2,11.9,52.0)	(46.7,1409.1,61.6) (9.8,40.5,4.7)	-1.662 0.012	0.210 0.022
<i>DTG - 4</i>	28	(18.2,2.5,65.8) (81.5,44.4,208.9)	(196.1,19.3,977.0) (143.5,293.3,104.0)	-1.631 0.053	0.475 0.154
<i>DTG - 5</i>	27	(-2.5,189.7,-25.8) (35.7,16.0,67.3)	(29.5,1392.6,105.7) (11.4,53.0,6.0)	-1.655 0.014	0.167 0.035
<i>DTG - 6</i>	24	(-0.8,237.5,-1.6) (15.2,4.4,8.9)	(3.4,1936.8,1.4) (1.9,12.0,0.9)	-1.551 0.004	0.050 0.014
<i>DTG - 7</i>	23	(29.8,15.1,-2.3) (75.8,16.6,36.6)	(573.1,107.5,31.5) (28.8,121.9,7.3)	-1.845 0.024	0.922 0.044
<i>DTG - 8</i>	23	(1.2,2.8,3.6) (144.0,9.5,30.3)	(826.9,24.6,38.5) (32.8,78.7,21.0)	-1.708 0.025	0.971 0.033
<i>DTG - 9</i>	23	(13.2,204.9,0.0) (22.0,4.2,10.3)	(21.3,1638.7,2.0) (4.9,14.0,1.2)	-1.632 0.003	0.134 0.015
<i>DTG - 10</i>	22	(-5.4,187.5,3.5) (19.4,2.7,8.4)	(45.2,1515.3,2.6) (4.4,25.5,1.6)	-1.661 0.009	0.199 0.009

NOTE—This table is a stub; the full table is available in the electronic edition.

**Table 5.** Identified Milky Way Substructures

MW Substructure	N Stars	$\langle [\text{Fe}/\text{H}] \rangle$	$\langle [\text{C}/\text{Fe}]_c \rangle$	$\langle [\alpha/\text{Fe}] \rangle$	$(\langle v_r \rangle, \langle v_\phi \rangle, \langle v_z \rangle)$	$(\langle J_r \rangle, \langle J_\phi \rangle, \langle J_z \rangle)$	$\langle E \rangle$	$\langle ecc \rangle$
					$(\sigma_{\langle v_r \rangle}, \sigma_{\langle v_\phi \rangle}, \sigma_{\langle v_z \rangle})$	$(\sigma_{\langle J_r \rangle}, \sigma_{\langle J_\phi \rangle}, \sigma_{\langle J_z \rangle})$	$\sigma_{\langle E \rangle}$	$\sigma_{\langle ecc \rangle}$
					(km s <sup>-1</sup> )	(kpc km s <sup>-1</sup> )	(10 <sup>5</sup> km <sup>2</sup> s <sup>-2</sup> )	
GSE	523	-1.556	+0.309	+0.315	(-9.6,10.5,-1.9)	(726.9,77.7,129.9)	-1.694	0.876
		0.532	0.442	0.177	(159.6,35.6,74.9)	(367.0,255.4,115.0)	0.151	0.089
MWTD	119	-1.386	+0.294	+0.355	(1.8,128.4,-7.2)	(202.8,933.9,130.3)	-1.717	0.459
		0.597	0.249	0.162	(74.6,36.4,75.7)	(88.0,222.3,95.1)	0.063	0.132
Splashed Disk	56	-1.109	+0.478	+0.516	(-0.5,182.3,-2.6)	(58.0,1358.0,67.0)	-1.673	0.228
		0.413	0.294	0.113	(38.6,19.5,49.1)	(30.9,65.4,47.3)	0.021	0.069
Thamnos	40	-2.004	+0.252	+0.364	(12.0,-124.3,-10.5)	(197.4,-822.0,125.9)	-1.761	0.482
		0.541	0.310	0.139	(75.0,30.5,67.5)	(78.0,193.4,86.5)	0.044	0.101
Helmi Stream	12	-1.950	+0.192	+0.360	(-23.1,140.9,-139.9)	(366.8,1098.2,1149.4)	-1.342	0.434
		0.548	0.255	0.082	(111.0,43.7,183.0)	(133.0,244.9,58.7)	0.054	0.065
LMS-1	10	-2.461	+0.366	+0.349	(62.5,49.1,3.9)	(595.7,346.7,1985.4)	-1.268	0.514
		0.411	0.369	0.173	(134.3,42.9,279.7)	(201.8,286.7,73.0)	0.055	0.077

tive azimuthal velocity component of the MWTD are all consistent with the velocity distribution for the MWTD from Carollo et al., even with the  $[\text{Fe}/\text{H}]$  cut containing more metal-rich stars than in their sample. The mean eccentricity distribution found within this substructure is also similar to that reported by Carollo et al., showing that the MWTD is a distinct component from the canonical thick disk (TD). Recently, both An & Beers (2020) and Dietz et al. (2021) have presented evidence that the MWTD is an independent structure from the TD. The distribution in  $\langle[\text{Fe}/\text{H}]\rangle$  and mean velocity space represents a stellar population consistent with the high-Mg population (Hayes et al. 2018), with the mean  $\alpha$ -element abundance being similar within errors. The  $\langle[\text{C}/\text{Fe}]_c\rangle$  abundance is also given for the MWTD, and shows an enhancement in carbon, possibly pointing to a relation with the strongly prograde CEMP structure found in Dietz et al. (2021), which was attributed to the MWTD population. Notice in Figure 11 how the MWTD occupies a higher energy component of the disk (the gray dots mostly positioned with prograde orbits) in the Lindblad diagram.

#### 4.1.3. *The Splashed Disk*

The third-most populated substructure is the Splashed Disk (SD), which contains 56 member stars. The SD is thought to be a component of the primordial MW disk that was kinematically heated during the GSE merger event (Helmi et al. 2018; Di Matteo et al. 2019; Belokurov et al. 2020). The mean velocity components of the SD are consistent with a null radial and vertical velocity, while showing a large positive azimuthal velocity consistent with disk-like stars. The mean eccentricity of these stars is consistent with disk-like orbits. The SD consists of the most metal-rich substructure identified here. The high  $\langle[\alpha/\text{Fe}]\rangle$  abundances for the SD shows that these stars are old, and they could be the result of a possible merger event, such as the one that created GSE. The  $\langle[\text{C}/\text{Fe}]_c\rangle$  abundance for the SD are high, which is in conjunction with the high mean  $\alpha$ -element abundances. Notice in Figure 11 how the SD overlaps with the MWTD. This is due to the selection criteria only using metallicity and  $\alpha$ -element abundances to determine the SD stars (Naidu et al. 2020). Considering the SD is thought to be composed of stars that have been heated due to the GSE merger event, the positions of the SD stars in the Lindblad diagram does not show a relatively large deviation from disk-like orbits. More associations with the SD are needed to make any definitive claims.

#### 4.1.4. *Thamnos*

The fourth-most populated substructure is Thamnos, which contains 40 member stars. Thamnos was proposed by Koppelman et al. (2019b) as a merger event that populated these stars in a retrograde orbit that is similar to TD stars. The low energy and strong retrograde rotation suggest that Thamnos merged with the MW long ago (Koppelman et al. 2019b). Here we find a similar low mean orbital energy and strong mean retrograde motion, and we recover as strong a retrograde motion as in Koppelman et al. (2019b), within errors. The low mean metallicity, consistent with the value reported by Limberg et al. (2021a), and elevated  $\langle[\text{C}/\text{Fe}]_c\rangle$  of these stars also supports the merger being ancient. The  $\langle[\alpha/\text{Fe}]\rangle$  is high, also suggesting an old population, consistent with Kordopatis et al. (2020). Notice in Figure 11 how Thamnos occupies a space that could be described as a retrograde version of disk stars.

#### 4.1.5. *The Helmi Stream*

The second-to-least populated substructure is the Helmi Stream (HS), which contains 12 member stars. The HS is one of the first detected dynamical substructures in the MW using integral of motions (Helmi et al. 1999). The HS has a characteristically high vertical velocity, which separates it from other stars that lie in the disk, and can be seen in the sample here. The large uncertainty on vertical velocity of the HS members corresponds to the positive and negative vertical velocity components of the stream, with the negative vertical velocity population dominating, consistent with the members determined here (Helmi 2020). The  $\langle[\text{Fe}/\text{H}]\rangle$  of the HS is more metal-poor in this sample, compared to the known HS members ( $[\text{Fe}/\text{H}] \sim -1.5$ ; Koppelman et al. 2019a). Recently however, Limberg et al. (2021c) noted that the metallicity range of HS is more metal-poor than previously expected, with stars reaching down to  $[\text{Fe}/\text{H}] \sim -2.5$ , which is consistent with the results presented here. Notice in Figure 11 how the HS occupies a relatively isolated space in the Lindblad diagram, thanks to the large vertical velocity of the stars providing the extra energy compared to the other disk stars.

#### 4.1.6. *LMS-1 (Wukong)*

The least populated substructure is LMS-1, which contains 10 member stars. LMS-1 was first identified by Yuan et al. (2020b), and was also detected by Naidu et al. (2020), who called it Wukong. This structure is similar to GSE in terms of the velocity component, but is characterized by a higher energy along with a more metal-poor population (Naidu et al. 2020), which is shown in the small number of stars representing LMS-1 in our sample. Notice in Figure 11 how LMS-1 overlaps

**Table 6.** Associations of Identified DTGs

Structure	Reference	Associations	Identified DTGs
MW Substructure	Naidu et al. (2020)	GSE	7, 8, 12, 17, 18, 20, 24, 26, 27, 28, 30, 44, 45, 46, 50 56, 57, 58, 66, 69, 70, 71, 75, 76, 78, 79, 80, 92, 95, 96 97, 98, 100, 111, 112, 113, 114, 115, 116, 133, 134, 135 136, 137, 141, 142, 146, 156, 164, 166, 167, 168, 169
		MWTD	14, 22, 29, 37, 43, 65, 90, 106, 107, 110, 132
		Thamnos	47, 52, 102, 138, 170
		Splashed Disk	5, 15, 86
		Helmi Stream	42
		LMS-1	67
		Ryu 879 (RLGC 2)	12, 57, 58
		IC 1257	66
		NGC 4833	7
		NGC 5139 ( $\omega$ Cen)	18
Globular Clusters	Vasiliev & Baumgardt (2021)	NGC 6284	141
		NGC 6356	52
		NGC 6397	55
		NGC 6752	33

with GSE in the Linblad Diagram, but these stars exhibit a lower eccentricity ( $ecc \sim 0.35$ ) compared to the GSE stars ( $ecc > 0.7$ ) forming their own distinct substructure, with a more clear division in the projected-action plot.

#### 4.2. Previously Identified Dynamically Tagged Groups and Stellar Associations

Separately, we can compare the newly identified DTGs in this work with other dynamical groups identified by previous authors. We take the mean group properties used to detect the previously identified groups and compare them to the mean and dispersion for the dynamical parameters of our identified DTGs. Stellar associations are also considered, allowing the identification of stars in our sample that belong to previously identified groups. For details on the previous work used in this process, see Paper I. The resulting dynamical associations between our identified DTGs and previously identified groups (along with substructure and globular cluster associations, see Section 4.3) are listed in Table 6. Table 2 lists the individual stellar associations for each of our DTGs.

One example of associations of identified DTGs with past groups is DTG-42. This DTG was associated with the Helmi Stream through the procedure outlined in Naidu et al. (2020) (see Section 4.1 for more details). There were four stars associated with this DTG through a  $5''$  radius search of the DTG member stars. Two of the stars belong in HK18:Green, and the other two belong in NB20:H99, both of which are associated with the Helmi Stream (Koppelman et al. 2018). DTG-42 is also dynamically associated with GM18a:S2, GM18b:S2, DG21:CDTG-15, and GL20:DTG-3, all of

which were identified as part of the Helmi Stream (Myeong et al. 2018a,b; Gudin et al. 2021; Limberg et al. 2021a). DG21:CDTG-15 was originally associated with GL20:DTG-3 as well by the authors, further strengthening our associations (Gudin et al. 2021).

An interesting DTG associated with the GSE is DTG-7, which has multiple previously identified groups and stars associated with them. Taking a closer look at DTG-7, we can find three stellar associations between this group and DG21:CDTG-1, and one stellar association each in IR18:E and EV21:NGC 4833, a globular cluster (Gudin et al. 2021; Roederer et al. 2018; Vasiliev & Baumgardt 2021). Again DG21:CDTG-1 is found associated with IR18:E by the authors, and even though we have a stellar association with EV21:NGC 4833, we do not find a strong dynamical association between DTG-7 and the globular cluster (Gudin et al. 2021; Vasiliev & Baumgardt 2021). DTG-7 is dynamically associated with GC21:Sausage, DG21:CDTG-1, GL21:DTG-37, DS21:DTG-43, again all of which are associated to GSE by their authors (Cordoni et al. 2021; Gudin et al. 2021; Limberg et al. 2021a; Shank et al. 2021).

The only DTG with multiple associations related to the MWTD is DTG-14. Stellar associations with DG21:CDTG-6 and HL19:GL-1 were found, with neither of them having associations to large-scale substructure by their authors (Gudin et al. 2021; Li et al. 2019). Dynamical associations with both HL19:GL-1 and DS21:DTG-2 are found with DTG-14. Interestingly, since we use the same procedure outlined by Shank et al. (2021), those authors found that DS21:DTG-2 is also associated with both HL19:GL-1 and DG21:CDTG-

6 along with the MWTD. These associations across multiple papers show how powerful these identifications are when identifying past structures, such as the unidentified DG21:CTDG-6 and HL19:GL-1 as candidate MWTD associations.

DTG-102 is an interesting case, since we have associated it with Thamnos, and there are 3 stellar associations with previously identified groups along with one dynamical association. There were two stellar associations between DTG-102 and HL20:GR-2, which was not identified by the authors (Li et al. 2020). DG21:CDTG-2 had a stellar association and was also dynamically associated with DTG-102 while being identified as a part of Thamnos by the authors (Gudin et al. 2021).

Finally, there is an unassigned MW substructure DTG that has multiple associations in DTG-4. DTG-4 has four stellar associations, two of which are to DG21:CDTG-18 and the other two are associated with DS21:DTG-4. Both of these are unassigned by the authors, but DS21:DTG-4 was found to have associations with GC21:Sausage, DG21:CDTG-14, and GL21:DTG-13, of which GC21:Sausage is tentatively associated to GSE, and DG21:CDTG-14 is unassigned, while GL21:DTG-13 is associated to ZY20:DTG-39 which is unassigned (Cordoni et al. 2021; Gudin et al. 2021; Limberg et al. 2021a; Yuan et al. 2020a). Dynamical associations with DTG-4 include GM18a:C1, HL19:GL-2, GL21:DTG-8, and DS21:DTG-4. Of these associated groups, GL21:DTG-8 and DS21:DTG-4 have previous associations by their authors. DS21:DTG-4 was already discussed in detail, while GL21:DTG-8 is previously associated to ZY20:DTG-35, which is also unassigned by their authors (Myeong et al. 2018a; Li et al. 2019; Limberg et al. 2021a; Shank et al. 2021). The DTGs that have unassigned MW substructure can offer valuable insights into the smaller structures of the MW that have yet to be confirmed.

Another use of the stellar associations comes from the suggestion by Roederer et al. (2018), strengthened by Gudin et al. (2021), that dynamical groups of stars have a statistically significant correlation between their elemental abundances. This is of importance to discover new chemically peculiar stars, particularly  $r$ -process-enhanced stars. Out of our DTGs, there are 22 associations between known  $r$ -process-enhanced stars and our discovered DTGs. The member stars in these DTGs

provide interesting candidates for high-resolution spectroscopic follow-up, due to the increased likelihood of the other members comprising chemically peculiar stars, especially in terms of  $r$ -process enhancement (Roederer et al. 2018; Gudin et al. 2021).

#### 4.3. Globular Clusters and Dwarf Galaxies

Both globular clusters and dwarf galaxies have been shown to play an important role in the formation of chemically peculiar stars (Ji et al. 2016; Myeong et al. 2018c). Globular clusters can also be a good indicator of galaxy-formation history based on their metallicities and orbits (Woody & Schlaufman 2021). From the work of Vasiliev & Baumgardt (2021), we can compare the dynamical properties of 170 globular clusters to those of the DTGs we identify. The procedure that is employed is the same one used for previously identified groups and stellar associations introduced in Sec. 4.2. The dynamics for 45 dwarf galaxies of the MW (excluding the Large Magellanic Cloud, Small Magellanic Cloud, and Sagittarius) are also explored. Paper I contains details of the orbits of the globular clusters and dwarf galaxies. The same procedure used for previously identified groups was then applied to determine whether a DTG was dynamically associated to the dwarf galaxy. Stellar associations were also determined for both globular clusters and dwarf galaxies in the same manner as previously identified groups.

The above comparison exercise led to 10 globular cluster associations, with 8 being unique. For a breakdown of which globular clusters are associated with our DTGs, see Table 6. Ryu 879 (RLGC 2) has three DTG associations which agree with each other in mean metallicity ( $\langle [Fe/H] \rangle \sim -1.7$ ). The mean metallicity agrees with the discovery of the globular cluster Ryu 879 (RLGC 2) within errors (Ryu & Lee 2018). The rest of the globular cluster associations are each associated with only one DTG in this work. We identify IC 1257, NGC 6284, and NGC 6356 through dynamical association, while NGC 4833, NGC 5139 ( $\omega$ Cen), NGC 6397, and NGC 6752 are identified through stellar association. Even though the matched stars in these globular clusters would have individually been associated with the globular cluster orbital parameters, the overall DTG did not possess sufficiently similar orbital characteristics to be associated.

**Table 7.** Associations of Identified DTGs with Previous Groups

Reference	Associations	Identified DTGs
Shank et al. (2021)	DTG-1	119, 147, 148
	DTG-2	14, 53
	DTG-17	17, 27
	DTG-29	20, 135
	DTG-3	8
	DTG-4	4
	DTG-5	26
	DTG-8	75
	DTG-9	55
	DTG-11	57
	DTG-12	10
	DTG-13	2
	DTG-14	163
	DTG-19	103
	DTG-22	133
	DTG-23	19
	DTG-27	28
	DTG-30	31
	DTG-36	95
	DTG-42	92
DTG-43	7	
DTG-44	90	
DTG-47	6	
Gudin et al. (2021)	CDTG-5	15, 176
	CDTG-7	79, 141
	CDTG-22	70, 164
	CDTG-23	25, 124
	CDTG-1	7
	CDTG-2	102
	CDTG-3	51
	CDTG-4	67
	CDTG-6	14
	CDTG-9	8
	CDTG-12	111
	CDTG-13	46
	CDTG-14	78
	CDTG-15	42
	CDTG-18	4
CDTG-19	20	
CDTG-28	30	
Limberg et al. (2021a)	DTG-37	7, 17, 71
	DTG-2	67
	DTG-3	42
	DTG-8	4
	DTG-11	92
	DTG-25	170
DTG-34	8	

*Table 7 continued*

**Table 7** (*continued*)

Reference	Associations	Identified DTGs
Helmi et al. (2017)	VelHel-6	26, 29, 44, 69, 70, 71, 93, 133, 166
	VelHel-7	94, 124, 132
	VelHel-2	98, 156
	VelHel-5	30, 46
	VelHel-1	98
	VelHel-4	47
Borsato et al. (2020)	Enc	50
	H99	42
Cordoni et al. (2021)	Sausage	7, 8, 17, 24, 28, 30, 45, 50, 57, 58, 66, 75 79, 80, 92, 98, 115, 134, 135, 136, 142, 146, 168
	Sequoia	47, 52, 127, 138
Li et al. (2019)	GL-1	14, 38, 99
	GL-2	4
Li et al. (2020)	GR-1	20, 27, 97, 114, 141
	GR-2	102, 138
Monty et al. (2020)	Sausage	28, 50, 66, 75, 92
	SeqG1	170
Myeong et al. (2018a)	C1	4, 67
	S2	42
Myeong et al. (2018b)	Cand11	67
	S2	42
Koppelman et al. (2018)	Green	42
Myeong et al. (2017)	Comoving	12, 58, 67, 75, 79, 80
Roederer et al. (2018)	E	7

NOTE—We draw attention to the associations with CDTGs from [Gudin et al. \(2021\)](#) and [Roederer et al. \(2018\)](#) due to their enhancement in  $r$ -process abundances.

The DTGs associated with globular clusters are expected to have formed in chemically similar birth environments; this is mostly supported through the similar chemical properties of the DTGs. Associations of globular clusters with Galactic substructure have been made by [Massari et al. \(2019\)](#). These authors did not analyze Ryu 879 (RLGC 2), since the globular cluster was only recently discovered at the time of the publication. IC 1257, NGC 6284, and NGC 4833 were identified to GSE by both our identification and [Massari et al. \(2019\)](#) (see DTG-66, DTG-141, and DTG-7 respectively). NGC 6356 was identified as Thamnos by our determinations, while [Massari et al. \(2019\)](#) found it to be associated to the main disk which we do not consider as part of the substructure routine, though it should be pointed out that Thamnos has the dynamics of a higher-energy retrograde disk similar to the MWTD ([Koppelman et al. 2019b](#)). NGC 5139 ( $\omega$  Cen) was identified as being associated with GSE or Sequoia by [Massari et al. \(2019\)](#), and our associations did recover this match to GSE (see DTG-18). NGC 6397 and NGC 6752 are not associated to any substructure by our procedure (see DTG-55 and DTG-33, respectively), but [Massari et al. \(2019\)](#) find

them associated to the main disk, which is not a part of the substructure routine.

We did not identify any associations of DTGs to the sample of (surviving) MW dwarf galaxies, either through stellar associations, or through the dynamical association procedure described above. Nevertheless, some of the DTGs identified by our analysis may well be associated with dwarf galaxies that have previously merged with the MW.

The analysis on the global properties of the identified DTGs that was explored in Section 6 of Paper I is foregone in this analysis due to the small number of DTGs that have sufficient C and  $\alpha$ -element abundances to derive meaningful conclusions. Attention to the small number of DTGs that do meet these requirements are listed in Table 3.

## 5. DISCUSSION

We have assembled a Full Sample of 8675 stars from the RAVE DR6 survey ([Steinmetz et al. 2020a](#)) with available estimates of  $[\text{Fe}/\text{H}]$ , and in some cases, with  $[\text{C}/\text{Fe}]$  and  $[\alpha/\text{Fe}]$ .

The Initial Sample contained 8377 stars, with  $4250 \leq T_{\text{eff}} \text{ (K)} \leq 7000$  and  $[\text{Fe}/\text{H}] \leq -0.8$ , 106 of which we identify as CEMP stars ( $[\text{C}/\text{Fe}]_c > +0.7$ ); these are listed in Table 10 in the Appendix. These stars are

of interest due to their enhanced carbon and association to morphological groups described in [Yoon et al. \(2016\)](#). Based on their classification scheme, there are approximately 50 Group I CEMP stars, 55 Group II CEMP stars, and 5 Group III CEMP stars, with a number of stars that have ambiguous classifications. This list provides a useful reference for high-resolution follow-up targets, some of which has already begun (e.g., [Rasmussen et al. 2020](#) and [Zepeda et al. 2021](#)).

The Final Sample of 7957 metal-poor stars had sufficient radial velocity and astrometric information from which orbits were constructed, in order to determine Dynamically Tagged Groups (DTGs) in orbital energy and cylindrical action space with the `HDBSCAN` algorithm. We chose `HDBSCAN` as the clustering algorithm due to precedence within the literature ([Koppelman et al. 2019b](#); [Gudin et al. 2021](#); [Limberg et al. 2021a](#); [Shank et al. 2021](#)), and its ability to extract clusters of stars over the energy and action space. Other clustering algorithms have been considered in the past, such as agglomerative clustering, affinity propagation, K-means, and mean-shift clustering ([Roederer et al. 2018](#)), along with friends-of-friends ([Gudin et al. 2021](#)).

We recover 179 DTGs that include between 5 and 35 members, with 67 DTGs containing at least 10 member stars. These DTGs were associated with MW substructure, resulting in the identification of the Gaia-Sausage-Enceladus, the Metal-Weak Thick Disk, the Splashed Disk, Thamnos, the Helmi Stream, and LMS-1 (Wukong). A total of 8 unique globular clusters were associated with 10 different DTGs, while no surviving dwarf galaxies were determined to be associated with the identified DTGs. Previously identified groups were found to be associated with the DTGs as well, with past work mostly confirming our substructure identification. Each of these associations allow insights into the dynamical and chemical properties of the parent substructures.

The implications of past group and stellar associations were explored with emphasis placed on the structure associations. Chemically peculiar stellar associations and previously identified Chemo-Dynamically Tagged Groups (CDTGs) were addressed as being good candidates for high-resolution follow-up spectroscopy targets, due to the statistical likelihood of the other members being chemically peculiar as well, mostly focused on  $r$ -process-enhanced stars.

The methods presented here will be used on larger samples of field stars that we are in the process of assembling – the HK/HES/HKII surveys ([Beers et al. 1985, 1992](#); [Christlieb et al. 2008](#); [Rhee 2001](#)) (a subset of which were analyzed by [Limberg et al. 2021a](#)), as well as SDSS/LAMOST and APOGEE. These data sets will

also be supplemented with photometric estimates of effective temperature and metallicity from [Huang et al. \(2021b\)](#), which allows stars from the HK/HES/HKII surveys with no previous spectroscopic follow-up to be explored, expanding the data set used by [Limberg et al. \(2021a\)](#).

## 6. APPENDIX

Here we present the tables for the Initial (Table 8) and Final (Table 9) Samples of the RAVE DR6 survey. We also present Table 10 which describes the identified CEMP stars and their associated morphological groups, according to the regions defined by [Yoon et al. \(2016\)](#).

**Table 8.** Description of the Initial Sample from the RAVE Survey

Column	Field	Unit	Description
1	RAVE ID	–	The RAVE DR6 RAVE ID of the star
2	Source ID	–	The Gaia EDR3 Source ID of the star
3	SMSS ID	–	The SMSS DR2 Source ID of the star
4	RAVE NAME	–	The RAVE DR6 RAVE NAME of the star
5	RA	(J2000)	The Right Ascension of the star given in hours:minutes:seconds
6	DEC	(J2000)	The Declination of the star given in degrees:minutes:seconds
7	Telescope	–	The telescope that was used to obtain the spectrum of the star
8	$V_{\text{mag}}$	–	The $V$ magnitude of the star as given by the $V_{\text{mag}}$ Reference
9	$G_{\text{mag}}$	–	The Gaia $G$ mean magnitude of the star as given by the Gaia Source ID
10	$G_{\text{BP}} - G_{\text{RP}}$	–	The Gaia BP – RP color mean magnitude of the star as given by the Gaia Source ID
11	$V_{\text{mag}}$ (Gaia)	–	The $V$ magnitude of the star as determined by the transformations from $G$ mag to $V$ mag using $V = G + 0.02704 - 0.01424 * (BP - RP) + 0.2156 * (BP - RP)^2 - 0.01426(BP - RP)^3$ given by <a href="#">Riello et al. (2021)</a>
12	$RV_{\text{RAVE}}$	( $\text{km s}^{-1}$ )	The radial velocity as given by the RAVE ID
13	Error	( $\text{km s}^{-1}$ )	The radial velocity error as given by the RAVE ID
14	$RV_{\text{Gaia}}$	( $\text{km s}^{-1}$ )	The radial velocity as given by the Gaia Source ID
15	Error	( $\text{km s}^{-1}$ )	The radial velocity error as given by the Gaia Source ID
16	Parallax	(mas)	The parallax as given by the Gaia Source ID
17	Error	(mas)	The parallax error as given by the Gaia Source ID
18	Distance	(kpc)	The inverse parallax distance (1/Parallax)
19	Error	(kpc)	The inverse parallax distance error ( $\text{Parallax}_{\text{error}}/(\text{Parallax}^2)$ )
20	Distance <sub>Corrected</sub>	(kpc)	The corrected inverse parallax distance ( $1/(\text{Parallax} + 0.026)$ ) based on <a href="#">Huang et al. (2021c)</a>
21	Error	(kpc)	The corrected inverse parallax distance error ( $\text{Parallax}_{\text{error}}/((\text{Parallax} + 0.026)^2)$ ) based on <a href="#">Huang et al. (2021c)</a>
22	Relative Error	–	The relative error of the corrected distance as given by Gaia
23	Distance BJ21	(kpc)	The 50 percentile distance as given by <a href="#">Bailer-Jones et al. (2021)</a> based on the Gaia Source ID
24	Error	(kpc)	The 50 percentile error as estimated by the 84 percentile distance and the 16 percentile distance as given by <a href="#">Bailer-Jones et al. (2021)</a> based on the Gaia Source ID ( $(\text{dist84}-\text{dist16})/2$ )
25	Relative Error	–	The relative error of the 50 percentile distance as given by <a href="#">Bailer-Jones et al. (2021)</a> based on the Gaia Source ID
26	Distance StarHorse	(kpc)	The 50 percentile distance as given by <a href="#">Anders et al. (2021)</a> based on the Gaia Source ID
27	Error	(kpc)	The 50 percentile error as estimated by the 84 percentile distance and the 16 percentile distance as given by <a href="#">Anders et al. (2021)</a> based on the Gaia Source ID ( $(\text{dist84}-\text{dist16})/2$ )
28	Relative Error	–	The relative error of the 50 percentile distance as given by <a href="#">Anders et al. (2021)</a> based on the Gaia Source ID
29	$PM_{\text{RA}}$	( $\text{mas yr}^{-1}$ )	The proper motion in the Right Ascension as given by the Gaia Source ID
30	Error	( $\text{mas yr}^{-1}$ )	The proper motion error in the Right Ascension as given by the Gaia Source ID
31	$PM_{\text{DEC}}$	( $\text{mas yr}^{-1}$ )	The proper motion in the Declination as given by the Gaia Source ID
32	Error	( $\text{mas yr}^{-1}$ )	The proper motion error in the Declination as given by the Gaia Source ID
33	Correlation Coefficient	–	The correlation coefficient between the proper motion in Right Ascension and the proper motion in Declination as given by the Gaia Source ID
34	$T_{\text{eff RAVE}}$	(K)	The effective temperature of the star as given by the RAVE ID
35	Error	(K)	The effective temperature error of the star as given by the RAVE ID
36	$T_{\text{eff Spec}}$	(K)	The effective temperature of the star as given by the n-SSPP
37	Error	(K)	The effective temperature error of the star as given by the n-SSPP
38	$T_{\text{eff Phot}}$	(K)	The effective temperature of the star as given by <a href="#">Huang et al. (2021b)</a>
39	Error	(K)	The effective temperature error of the star as given by <a href="#">Huang et al. (2021b)</a>
40	$T_{\text{eff}}$	(K)	The adopted effective temperature of the star based on the Parameter Procedure
41	Error	(K)	The adopted effective temperature error of the star based on the Parameter Procedure
42	$\log g_{\text{RAVE}}$	(cgs)	The surface gravity of the star as given by the RAVE ID
43	Error	(cgs)	The surface gravity error of the star as given by the RAVE ID
44	$\log g_{\text{Spec}}$	(cgs)	The surface gravity of the star as given by the n-SSPP

**Table 8** continued

Table 8 (continued)

Column	Field	Unit	Description
45	Error	(cgs)	The surface gravity error of the star as given by the n-SSPP
46	$\log g$	(cgs)	The adopted surface gravity of the star based on the Parameter Procedure
47	Error	(cgs)	The adopted surface gravity error of the star based on the Parameter Procedure
48	[M/H]	–	The metallicity of the star as given by the RAVE ID
49	Error	–	The metallicity error of the star as given by the RAVE ID
50	$[\text{Fe}/\text{H}]_{\text{Spec}}$	–	The metallicity of the star as given by the n-SSPP
51	Error	–	The metallicity error of the star as given by the n-SSPP
52	$[\text{Fe}/\text{H}]_{\text{Phot}}$	–	The metallicity of the star as given by <a href="#">Huang et al. (2021b)</a>
53	Error	–	The metallicity error of the star as given by <a href="#">Huang et al. (2021b)</a>
54	[Fe/H]	–	The adopted metallicity of the star based on the Parameter Procedure
55	Error	–	The adopted metallicity error of the star based on the Parameter Procedure
56	[C/Fe]	–	The carbon abundance ratio for the star
57	Error	–	The carbon abundance ratio error for the star
58	$[\text{C}/\text{Fe}]_c$	–	The carbon abundance corrected for evolutionary effects from <a href="#">Placco et al. (2014)</a>
59	$\text{AC}_c$	–	The absolute carbon corrected for evolutionary effects from <a href="#">Placco et al. (2014)</a> ( $[\text{C}/\text{Fe}]_c + [\text{Fe}/\text{H}] + \log(\epsilon)_{\text{Carbon,Solar}}$ ) (Taken from solar value of 8.43 from <a href="#">Asplund et al. (2009)</a> )
60	CARDET	–	Flag with “D” if the carbon abundance ( $[\text{C}/\text{Fe}]$ ) is detected from n-SSPP and “U” if an upper limit by n-SSPP and “L” if a lower limit by n-SSPP and “N” if none is detected by n-SSPP
61	$\text{CC}_{[\text{C}/\text{Fe}]}$	–	The correlation coefficient of $[\text{C}/\text{Fe}]$ as given by the n-SSPP
62	CEMP	–	Flag as “C” for Carbon-Enhanced Metal-Poor (CEMP) if $[\text{C}/\text{Fe}]_c > +0.7$ and “I” for CEMP-intermediate if $+0.5 < [\text{C}/\text{Fe}]_c \leq +0.7$ and “N” for Carbon-Normal if $[\text{C}/\text{Fe}]_c \leq +0.5$ and “X” if there is no $[\text{C}/\text{Fe}]_c$ information
63	$[\alpha/\text{Fe}]_{\text{RAVE}}$	–	The alpha-element abundance ratio for the star as given by the RAVE ID
64	Error	–	The alpha-element abundance ratio error for the star as given by the RAVE ID
65	$[\alpha/\text{Fe}]_{\text{Spec}}$	–	The alpha-element abundance ratio for the star as given by the n-SSPP
66	Error	–	The alpha-element abundance ratio error for the star as given by the n-SSPP
67	ALPDET	–	Flag with “D” if the alpha abundance ( $[\alpha/\text{Fe}]$ ) is detected from n-SSPP and “U” if an upper limit by n-SSPP and “L” if a lower limit by n-SSPP and “N” if none is detected by n-SSPP
68	$\text{CC}_{[\alpha/\text{Fe}]}$	–	The correlation coefficient of $[\alpha/\text{Fe}]$ as detected by the n-SSPP
69	$[\alpha/\text{Fe}]$	–	The alpha-element abundance ratio for the star based on the Parameter Procedure
70	Error	–	The alpha-element abundance ratio error for the star based on the Parameter Procedure
71	SNR	–	The average Signal-to-Noise Ratio of the spectrum from the RAVE ID
72	Reference	–	The Reference for the star as given by “RAVE DR6” for the sample of stars from <a href="#">Steinmetz et al. (2020a)</a> sample and “RAVE DR5” for the sample of stars from <a href="#">Kunder et al. (2017)</a>
73	Parameter Procedure	–	The procedure used to determine the adopted stellar parameters ( $T_{\text{eff}}$ , $\log g$ , $[\text{Fe}/\text{H}]$ , and $[\alpha/\text{Fe}]$ ) (“Average” is used if the difference between $[\text{Fe}/\text{H}]_{\text{Spec}}$ and $[\text{Fe}/\text{H}]_{\text{Phot}}$ is less $\leq 0.5$ dex and “Spectroscopic” is used if only $[\text{Fe}/\text{H}]_{\text{Spec}}$ is available and “Photometric” is used if only $[\text{Fe}/\text{H}]_{\text{Phot}}$ is available, while a choice is made between $[\text{Fe}/\text{H}]_{\text{Spec}}$ and $[\text{Fe}/\text{H}]_{\text{Phot}}$ if both are available and the difference is $> 0.5$ dex)
74	$V_{\text{mag}}$ Reference	–	The Reference for the $V$ magnitude of the star
75	Distance AGAMA	–	The Reference for the distance used in AGAMA (StarHorse prioritized over BJ21 unless StarHorse distance has relative error greater than 0.3, if both have a relative error greater than 0.3 we adopt no distance estimate)
76	RV Reference	–	The Reference for the RV

**Table 9.** Description of the Final Sample from the RAVE Survey

Column	Field	Unit	Description
1	RAVE ID	–	The RAVE DR6 RAVE ID of the star
2	Source ID	–	The Gaia EDR3 Source ID of the star
3	SMSS ID	–	The SMSS DR2 Source ID of the star
4	RAVE NAME	–	The RAVE DR6 RAVE NAME of the star
5	RA	(J2000)	The Right Ascension of the star given in hours:minutes:seconds
6	DEC	(J2000)	The Declination of the star given in degrees:minutes:seconds
7	Telescope	–	The telescope that was used to obtain the spectrum of the star
8	$V_{\text{mag}}$	–	The $V$ magnitude of the star as given by the $V_{\text{mag}}$ Reference
9	$G_{\text{mag}}$	–	The Gaia $G$ mean magnitude of the star as given by the Gaia Source ID
10	$G_{\text{BP}} - G_{\text{RP}}$	–	The Gaia BP – RP color mean magnitude of the star as given by the Gaia Source ID
11	$V_{\text{mag}}$ (Gaia)	–	The $V$ magnitude of the star as determined by the transformations from $G$ mag to $V$ mag using $V = G + 0.02704 - 0.01424 * (BP - RP) + 0.2156 * (BP - RP)^2 - 0.01426(BP - RP)^3$ given by <a href="#">Riello et al. (2021)</a>
12	$RV_{\text{RAVE}}$	( $\text{km s}^{-1}$ )	The radial velocity as given by the RAVE ID
13	Error	( $\text{km s}^{-1}$ )	The radial velocity error as given by the RAVE ID
14	$RV_{\text{Gaia}}$	( $\text{km s}^{-1}$ )	The radial velocity as given by the Gaia Source ID
15	Error	( $\text{km s}^{-1}$ )	The radial velocity error as given by the Gaia Source ID
16	Parallax	(mas)	The parallax as given by the Gaia Source ID
17	Error	(mas)	The parallax error as given by the Gaia Source ID
18	Distance	(kpc)	The inverse parallax distance ( $1/\text{Parallax}$ )
19	Error	(kpc)	The inverse parallax distance error ( $\text{Parallax}_{\text{error}}/(\text{Parallax}^2)$ )
20	Distance <sub>Corrected</sub>	(kpc)	The corrected inverse parallax distance ( $1/(\text{Parallax} + 0.026)$ ) based on <a href="#">Huang et al. (2021c)</a>
21	Error	(kpc)	The corrected inverse parallax distance error ( $\text{Parallax}_{\text{error}}/((\text{Parallax} + 0.026)^2)$ ) based on <a href="#">Huang et al. (2021c)</a>
22	Relative Error	–	The relative error of the corrected distance as given by Gaia
23	Distance BJ21	(kpc)	The 50 percentile distance as given by <a href="#">Bailer-Jones et al. (2021)</a> based on the Gaia Source ID
24	Error	(kpc)	The 50 percentile error as estimated by the 84 percentile distance and the 16 percentile distance as given by <a href="#">Bailer-Jones et al. (2021)</a> based on the Gaia Source ID ( $(\text{dist}_{84} - \text{dist}_{16})/2$ )
25	Relative Error	–	The relative error of the 50 percentile distance as given by <a href="#">Bailer-Jones et al. (2021)</a> based on the Gaia Source ID
26	Distance StarHorse	(kpc)	The 50 percentile distance as given by <a href="#">Anders et al. (2021)</a> based on the Gaia Source ID
27	Error	(kpc)	The 50 percentile error as estimated by the 84 percentile distance and the 16 percentile distance as given by <a href="#">Anders et al. (2021)</a> based on the Gaia Source ID ( $(\text{dist}_{84} - \text{dist}_{16})/2$ )
28	Relative Error	–	The relative error of the 50 percentile distance as given by <a href="#">Anders et al. (2021)</a> based on the Gaia Source ID
29	$PM_{\text{RA}}$	( $\text{mas yr}^{-1}$ )	The proper motion in the Right Ascension as given by the Gaia Source ID
30	Error	( $\text{mas yr}^{-1}$ )	The proper motion error in the Right Ascension as given by the Gaia Source ID
31	$PM_{\text{DEC}}$	( $\text{mas yr}^{-1}$ )	The proper motion in the Declination as given by the Gaia Source ID
32	Error	( $\text{mas yr}^{-1}$ )	The proper motion error in the Declination as given by the Gaia Source ID
33	Correlation Coefficient	–	The correlation coefficient between the proper motion in Right Ascension and the proper motion in Declination as given by the Gaia Source ID
34	$T_{\text{eff RAVE}}$	(K)	The effective temperature of the star as given by the RAVE ID
35	Error	(K)	The effective temperature error of the star as given by the RAVE ID
36	$T_{\text{eff Spec}}$	(K)	The effective temperature of the star as given by the n-SSPP
37	Error	(K)	The effective temperature error of the star as given by the n-SSPP
38	$T_{\text{eff Phot}}$	(K)	The effective temperature of the star as given by <a href="#">Huang et al. (2021b)</a>
39	Error	(K)	The effective temperature error of the star as given by <a href="#">Huang et al. (2021b)</a>
40	$T_{\text{eff}}$	(K)	The adopted effective temperature of the star based on the Parameter Procedure
41	Error	(K)	The adopted effective temperature error of the star based on the Parameter Procedure
42	$\log g_{\text{RAVE}}$	(cgs)	The surface gravity of the star as given by the RAVE ID
43	Error	(cgs)	The surface gravity error of the star as given by the RAVE ID
44	$\log g_{\text{Spec}}$	(cgs)	The surface gravity of the star as given by the n-SSPP

Table 9 continued

Table 9 (continued)

Column	Field	Unit	Description
45	Error	(cgs)	The surface gravity error of the star as given by the n-SSPP
46	$\log g$	(cgs)	The adopted surface gravity of the star based on the Parameter Procedure
47	Error	(cgs)	The adopted surface gravity error of the star based on the Parameter Procedure
48	[M/H]	–	The metallicity of the star as given by the RAVE ID
49	Error	–	The metallicity error of the star as given by the RAVE ID
50	$[\text{Fe}/\text{H}]_{\text{Spec}}$	–	The metallicity of the star as given by the n-SSPP
51	Error	–	The metallicity error of the star as given by the n-SSPP
52	$[\text{Fe}/\text{H}]_{\text{Phot}}$	–	The metallicity of the star as given by <a href="#">Huang et al. (2021b)</a>
53	Error	–	The metallicity error of the star as given by <a href="#">Huang et al. (2021b)</a>
54	[Fe/H]	–	The adopted metallicity of the star based on the Parameter Procedure
55	Error	–	The adopted metallicity error of the star based on the Parameter Procedure
56	[C/Fe]	–	The carbon abundance ratio for the star
57	Error	–	The carbon abundance ratio error for the star
58	$[\text{C}/\text{Fe}]_c$	–	The carbon abundance corrected for evolutionary effects from <a href="#">Placco et al. (2014)</a>
59	$\text{AC}_c$	–	The absolute carbon corrected for evolutionary effects from <a href="#">Placco et al. (2014)</a> ( $[\text{C}/\text{Fe}]_c + [\text{Fe}/\text{H}] + \log(\epsilon)_{\text{Carbon,Solar}}$ ) (Taken from solar value of 8.43 from <a href="#">Asplund et al. (2009)</a> )
60	CARDET	–	Flag with “D” if the carbon abundance ( $[\text{C}/\text{Fe}]$ ) is detected from n-SSPP and “U” if an upper limit by n-SSPP and “L” if a lower limit by n-SSPP and “N” if none is detected by n-SSPP
61	$\text{CC}_{[\text{C}/\text{Fe}]}$	–	The correlation coefficient of $[\text{C}/\text{Fe}]$ as given by the n-SSPP
62	CEMP	–	Flag as “C” for Carbon-Enhanced Metal-Poor (CEMP) if $[\text{C}/\text{Fe}]_c > +0.7$ and “I” for CEMP-intermediate if $+0.5 < [\text{C}/\text{Fe}]_c \leq +0.7$ and “N” for Carbon-Normal if $[\text{C}/\text{Fe}]_c \leq +0.5$ and “X” if there is no $[\text{C}/\text{Fe}]_c$ information
63	$[\alpha/\text{Fe}]_{\text{RAVE}}$	–	The alpha-element abundance ratio for the star as given by the RAVE ID
64	Error	–	The alpha-element abundance ratio error for the star as given by the RAVE ID
65	$[\alpha/\text{Fe}]_{\text{Spec}}$	–	The alpha-element abundance ratio for the star as given by the n-SSPP
66	Error	–	The alpha-element abundance ratio error for the star as given by the n-SSPP
67	ALPDET	–	Flag with “D” if the alpha abundance ( $[\alpha/\text{Fe}]$ ) is detected from n-SSPP and “U” if an upper limit by n-SSPP and “L” if a lower limit by n-SSPP and “N” if none is detected by n-SSPP
68	$\text{CC}_{[\alpha/\text{Fe}]}$	–	The correlation coefficient of $[\alpha/\text{Fe}]$ as detected by the n-SSPP
69	$[\alpha/\text{Fe}]$	–	The alpha-element abundance ratio for the star based on the Parameter Procedure
70	Error	–	The alpha-element abundance ratio error for the star based on the Parameter Procedure
71	SNR	–	The average Signal-to-Noise Ratio of the spectrum from the RAVE ID
72	Reference	–	The Reference for the star as given by “RAVE DR6” for the sample of stars from <a href="#">Steinmetz et al. (2020a)</a> sample and “RAVE DR5” for the sample of stars from <a href="#">Kunder et al. (2017)</a>
73	Parameter Procedure	–	The procedure used to determine the adopted stellar parameters ( $T_{\text{eff}}$ , $\log g$ , $[\text{Fe}/\text{H}]$ , and $[\alpha/\text{Fe}]$ ) (“Average” is used if the difference between $[\text{Fe}/\text{H}]_{\text{Spec}}$ and $[\text{Fe}/\text{H}]_{\text{Phot}}$ is less $\leq 0.5$ dex and “Spectroscopic” is used if only $[\text{Fe}/\text{H}]_{\text{Spec}}$ is available and “Photometric” is used if only $[\text{Fe}/\text{H}]_{\text{Phot}}$ is available, while a choice is made between $[\text{Fe}/\text{H}]_{\text{Spec}}$ and $[\text{Fe}/\text{H}]_{\text{Phot}}$ if both are available and the difference is $> 0.5$ dex)
74	$V_{\text{mag}}$ Reference	–	The Reference for the $V$ magnitude of the star
75	Distance AGAMA	–	The Reference for the distance used in AGAMA (StarHorse prioritized over BJ21 unless StarHorse distance has relative error greater than 0.3, if both have a relative error greater than 0.3 we adopt no distance estimate)
76	RV Reference	–	The Reference for the RV
77	$(v_r, v_\phi, v_z)$	(km s <sup>-1</sup> )	The cylindrical velocities of the star as given by AGAMA
78	Error	(km s <sup>-1</sup> )	The cylindrical velocity errors of the star as given by Monte Carlo sampling through AGAMA
79	$(J_r, J_\phi, J_z)$	(kpc km s <sup>-1</sup> )	The cylindrical actions of the star as given by AGAMA
80	Error	(kpc km s <sup>-1</sup> )	The cylindrical action errors of the star as given by Monte Carlo sampling through AGAMA
81	Energy	(km <sup>2</sup> s <sup>-2</sup> )	The orbital energy of the star as given by AGAMA

Table 9 continued

**Table 9** (*continued*)

Column	Field	Unit	Description
82	Error	( $\text{km}^2 \text{s}^{-2}$ )	The orbital energy error of the star as given by Monte Carlo sampling through AGAMA
83	$r_{\text{peri}}$	(kpc)	The Galactic pericentric distance of the star as given by AGAMA
84	Error	(kpc)	The Galactic pericentric distance error of the star as given by Monte Carlo sampling through AGAMA
85	$r_{\text{apo}}$	(kpc)	The Galactic apocentric distance of the star as given by AGAMA
86	Error	(kpc)	The Galactic apocentric distance error of the star as given by Monte Carlo sampling through AGAMA
87	$Z_{\text{max}}$	(kpc)	The maximum height above the Galactic plane of the star as given by AGAMA
88	Error	(kpc)	The maximum height above the Galactic plane error of the star as given by Monte Carlo sampling through AGAMA
89	Eccentricity	–	The eccentricity of the star given by $(r_{\text{apo}} - r_{\text{peri}})/(r_{\text{apo}} + r_{\text{peri}})$ through AGAMA
90	Error	–	The eccentricity error of the star as given by Monte Carlo sampling through AGAMA

**Table 10.** Identified CEMP stars and their Group Association

Name	Group	$T_{\text{eff}}$ (K)	$\log g$	[Fe/H]	[C/Fe]	[C/Fe] <sub>c</sub>	AC <sub>c</sub>	[ $\alpha$ /Fe]
J000022.60–130228.0	II	4874	1.451	–2.936	+0.531	+0.951	6.445	+0.206
J002330.69–163143.2	II	5590	2.801	–2.474	+0.785	+0.795	6.751	+0.298
J004539.31–745729.4	I	5049	1.800	–2.242	+1.025	+1.185	7.373	–0.015
J011522.35–802241.1	...	4682	1.286	–2.484	+0.151	+0.701	6.647	+0.420
J012931.10–160046.0	II	5096	1.591	–2.707	+0.533	+0.853	6.576	+0.343
J013346.60–272737.0	I	4821	1.324	–2.787	+2.317	+2.447	8.090	+0.600
J014738.05–113047.6	II	4874	1.514	–2.897	+0.705	+1.075	6.608	...
J023240.43–370811.2	II	4784	0.871	–2.554	+0.088	+0.758	6.634	...
J023558.70–674552.0	I	4718	1.326	–2.121	+1.470	+1.600	7.909	+1.006
J024010.80–141630.0	I	5952	2.387	–2.068	+2.159	+2.179	8.541	+0.547
J024620.10–151842.0	II	4943	1.395	–2.882	+0.423	+0.893	6.441	+0.373
J025007.20–514515.0	I	4550	0.936	–3.015	+0.938	+1.518	6.933	...
J032115.90–801824.0	I	4550	1.081	–2.281	+0.475	+0.965	7.114	...
J034236.50–133553.0	I/III	6375	2.910	–3.222	+1.699	+1.709	6.917	...
J040618.20–030525.0	I	5024	1.444	–2.088	+0.545	+0.885	7.227	...
J041716.50–033631.0	I	4712	0.844	–2.891	+1.421	+1.821	7.360	+0.104
J042314.50+013048.0	II	5109	1.681	–2.821	+0.589	+0.829	6.438	+0.206
J043831.80–705319.0	I	5043	1.758	–2.355	+0.557	+0.797	6.872	...
J044208.20–342114.0	I	4676	0.811	–3.084	+2.096	+2.346	7.692	...
J044240.00–104324.0	II	6012	3.216	–2.597	+0.931	+0.941	6.774	...
J045322.60–221040.0	I/II	6322	3.265	–2.336	+0.980	+0.990	7.084	...
J050947.56–442316.8	I	5932	3.824	–2.218	+0.940	+0.940	7.152	+0.445
J052029.30–582530.0	II	4819	0.948	–3.023	+0.100	+0.820	6.227	...
J055142.20–332734.0	II	4964	1.247	–2.578	+0.284	+0.824	6.676	...
J055736.90–512721.0	I	4710	0.913	–3.015	+2.228	+2.408	7.823	...
J060516.00–490728.0	I	6923	3.250	–1.151	+1.109	+1.119	8.398	...
J060554.00–330629.0	I	5315	2.465	–2.155	+1.340	+1.360	7.635	+0.321
J060555.10–485437.0	...	5302	3.145	–2.382	+0.719	+0.729	6.777	+0.300
J061950.00–531212.0	I	5414	2.398	–2.107	+0.709	+0.719	7.042	...
J065929.50–540613.0	I	4794	1.240	–2.338	+0.619	+1.049	7.141	...
J070520.28–334324.3	I/II	5050	1.652	–2.367	+0.531	+0.841	6.904	...
J085805.90–080917.0	II	4775	0.975	–3.136	+0.339	+1.039	6.333	+0.525
J091348.80–091909.0	I	7215	2.288	–1.858	+0.789	+0.799	7.371	+0.600
J092556.55–345037.3	I	6676	4.054	–2.530	+1.480	+1.480	7.380	...
J094921.83–161722.0	I	4757	1.424	–2.793	+1.213	+1.553	7.190	+0.789
J100800.70–100852.0	I/II	4571	0.848	–2.747	+0.494	+1.094	6.777	...
J101621.57–295952.1	I	5060	1.545	–2.085	+0.453	+0.783	7.128	...
J104410.96–035856.3	I	6337	3.215	–2.223	+1.563	+1.573	7.780	+0.511
J111912.33–160946.8	I	4988	1.377	–2.844	+1.168	+1.528	7.114	...
J112229.90–245854.0	I	4761	2.574	–1.087	+0.930	+0.950	8.293	...
J112243.40–020937.0	I/II	6377	3.278	–2.748	+1.144	+1.144	6.826	...
J114638.83–042239.5	I	4326	0.433	–2.322	+0.177	+0.777	6.885	+0.274
J114650.70–140643.0	III	6434	2.033	–3.412	+1.616	+1.626	6.644	...
J114948.00–081721.0	I	5706	1.419	–3.035	+2.636	+2.746	8.141	+0.715
J115337.30–020037.0	I/II	5146	2.315	–2.593	+1.012	+1.032	6.869	+0.211
J115801.30–152218.0	II	5038	1.819	–2.953	+0.605	+0.745	6.222	...
J121000.70–313036.0	II	4914	1.195	–2.570	+0.273	+0.833	6.693	...
J121920.34–172154.6	II	5070	1.815	–2.657	+0.536	+0.706	6.479	+0.365
J123550.13–313111.2	II	5123	2.224	–2.428	+0.789	+0.799	6.801	+0.272
J124537.80–092704.0	I	5450	3.288	–1.744	+0.817	+0.827	7.513	+0.478
J124718.30–555047.0	I	4917	1.678	–2.090	+1.347	+1.467	7.807	+0.052
J125728.30–512522.0	...	4985	1.513	–2.356	+0.294	+0.724	6.798	...

*Table 10 continued*

Table 10 (*continued*)

Name	Group	$T_{\text{eff}}$ (K)	$\log g$	[Fe/H]	[C/Fe]	[C/Fe] <sub>c</sub>	AC <sub>c</sub>	[ $\alpha$ /Fe]
J130119.30–454552.0	...	4769	0.767	−2.417	+0.050	+0.710	6.723	...
J130744.20–154542.0	I/II	6210	3.035	−2.405	+0.820	+0.830	6.855	+0.257
J132418.00–280356.0	I/II	4757	1.167	−2.589	+0.717	+1.197	7.038	...
J132918.40–025739.0	I	7147	3.168	−1.269	+1.100	+1.120	8.281	+0.600
J133245.30–240326.0	II	4589	0.419	−2.440	+0.087	+0.747	6.737	...
J134603.40–052414.0	II	5372	2.880	−2.831	+0.855	+0.865	6.464	+0.535
J135439.20–412746.0	I	5072	1.745	−2.278	+0.546	+0.786	6.938	...
J140230.10–053905.0	II/III	6504	3.582	−3.067	+1.259	+1.259	6.622	+0.187
J141126.20–113746.0	II	4301	0.658	−3.308	+0.237	+0.977	6.099	+0.546
J143811.20–212009.0	II	4542	1.186	−2.860	+0.556	+1.106	6.676	...
J143926.81–194913.3	I	5000	1.512	−2.830	+1.365	+1.645	7.245	...
J151335.50–124434.4	II	5097	1.776	−2.846	+0.593	+0.743	6.327	+0.144
J151919.20–083234.0	I/II	6507	4.032	−2.364	+0.899	+0.899	6.965	+0.182
J152140.00–353810.0	II	6029	3.024	−2.955	+1.151	+1.161	6.636	+0.928
J152713.50–233618.0	I	6255	4.199	−1.973	+0.765	+0.765	7.222	+0.297
J155751.80–083955.0	II	4572	0.699	−2.684	+0.377	+0.987	6.733	...
J155846.99–033950.8	I/II	5216	1.994	−2.685	+1.224	+1.264	7.009	...
J160334.40–062337.0	III	4548	1.494	−3.314	+1.260	+1.650	6.766	...
J161156.70–803442.0	I/II	4467	0.842	−2.419	+0.619	+1.109	7.120	+0.437
J162051.23–091258.0	II	4908	1.589	−3.103	+0.415	+0.755	6.082	+0.325
J165143.93–202926.5	...	6388	2.245	−2.360	+0.740	+0.750	6.820	...
J171800.40–033535.0	I	7766	4.731	−1.492	+0.933	+0.933	7.871	...
J171813.40–682301.0	II	4926	1.364	−2.563	+0.200	+0.720	6.587	...
J173600.10–514530.0	...	4862	1.012	−2.356	+0.109	+0.749	6.823	...
J180242.30–440443.0	II	4463	0.732	−2.749	+0.279	+0.919	6.600	...
J190733.10–415832.0	II	4602	1.110	−2.753	+0.088	+0.758	6.435	...
J192325.19–583340.9	I	5056	1.661	−2.396	+0.984	+1.214	7.248	...
J193204.50–730918.0	II	4300	0.308	−3.683	+0.674	+1.404	6.151	...
J194318.70–594819.9	I	5225	1.882	−2.228	+0.741	+0.861	7.063	−0.095
J194411.10–111927.0	I	5418	0.784	−2.185	+0.172	+0.752	6.997	+0.814
J194813.29–490344.8	II	4830	1.090	−2.486	+0.135	+0.765	6.709	...
J195637.98–793124.0	I	6150	3.545	−0.930	+1.041	+1.041	8.541	+0.439
J200630.40–490004.0	I	6368	4.370	−1.611	+0.887	+0.887	7.706	+0.233
J201446.10–563530.0	I	4785	1.334	−2.849	+1.387	+1.707	7.288	+0.547
J202434.50–423334.0	II	5394	3.155	−2.633	+0.901	+0.911	6.708	+0.469
J202602.40–474029.0	II	5041	1.650	−2.542	+0.475	+0.785	6.673	...
J203622.60–071420.0	II	4191	0.203	−2.882	+0.236	+0.916	6.464	+0.212
J203706.40–122125.0	II	4562	1.048	−2.860	+0.334	+0.974	6.544	+0.141
J203740.42–552050.0	II	4912	1.008	−2.811	+0.476	+1.086	6.705	...
J203843.20–002333.0	II	4746	0.735	−3.263	−0.035	+0.735	5.902	+0.426
J204406.30–300007.0	I	6059	3.350	−2.286	+0.788	+0.788	6.932	−0.145
J204450.70–371400.0	II	4507	0.717	−3.023	+0.341	+1.021	6.428	+0.266
J210540.70–452057.0	II	5074	1.778	−2.637	+0.601	+0.771	6.564	...
J210634.70–495750.0	II	5849	3.366	−2.549	+0.839	+0.839	6.720	...
J210642.94–682826.7	II	5401	3.696	−2.918	+1.019	+1.019	6.531	+0.659
J210958.10–094540.0	II	4625	0.542	−3.129	−0.049	+0.711	6.012	+0.501
J211525.50–150331.0	I/II	4622	0.728	−2.601	+0.504	+1.074	6.903	+0.818
J214055.30–101223.0	I	7782	3.010	−0.988	+1.529	+1.549	8.991	...
J222203.45–802459.3	II	4799	1.500	−2.895	+0.442	+0.842	6.377	+0.236
J222236.00–013827.1	II/III	5197	2.377	−3.049	+1.251	+1.261	6.642	+0.286
J223733.20–434118.0	II	5079	1.714	−2.406	+0.511	+0.781	6.805	...
J224601.31–593804.5	II	4584	0.905	−2.543	+0.152	+0.802	6.689	+0.483
J225319.90–224856.0	I	4864	1.167	−2.312	+1.402	+1.572	7.690	+0.465
J233107.20–022330.0	I	4867	1.423	−3.292	+2.449	+2.609	7.747	+0.600

NOTE—The CEMP Groups are given in [Yoon et al. \(2016\)](#).

## REFERENCES

- Abolfathi, B., Aguado, D. S., Aguilar, G., et al. 2018, *ApJS*, 235, 42, doi: [10.3847/1538-4365/aa9e8a](https://doi.org/10.3847/1538-4365/aa9e8a)
- Aguado, D. S., Youakim, K., González Hernández, J. I., et al. 2019, *MNRAS*, 490, 2241, doi: [10.1093/mnras/stz2643](https://doi.org/10.1093/mnras/stz2643)
- Ahumada, R., Prieto, C. A., Almeida, A., et al. 2020, *ApJS*, 249, 3, doi: [10.3847/1538-4365/ab929e](https://doi.org/10.3847/1538-4365/ab929e)
- An, D., & Beers, T. C. 2020, *ApJ*, 897, 39, doi: [10.3847/1538-4357/ab8d39](https://doi.org/10.3847/1538-4357/ab8d39)
- Anders, F., Khalatyan, A., Queiroz, A. B. A., et al. 2021, arXiv e-prints, arXiv:2111.01860. <https://arxiv.org/abs/2111.01860>
- Antoja, T., Helmi, A., Bienayme, O., et al. 2012, *MNRAS*, 426, L1, doi: [10.1111/j.1745-3933.2012.01310.x](https://doi.org/10.1111/j.1745-3933.2012.01310.x)
- Asplund, M., Grevesse, N., Sauval, A. J., & Scott, P. 2009, *ARA&A*, 47, 481, doi: [10.1146/annurev.astro.46.060407.145222](https://doi.org/10.1146/annurev.astro.46.060407.145222)
- Bailer-Jones, C. A. L., Rybizki, J., Fouesneau, M., Demleitner, M., & Andrae, R. 2021, *AJ*, 161, 147, doi: [10.3847/1538-3881/abd806](https://doi.org/10.3847/1538-3881/abd806)
- Beers, T. C., Flynn, K., & Gebhardt, K. 1990, *AJ*, 100, 32, doi: [10.1086/115487](https://doi.org/10.1086/115487)
- Beers, T. C., Norris, J. E., Placco, V. M., et al. 2014, *ApJ*, 794, 58, doi: [10.1088/0004-637X/794/1/58](https://doi.org/10.1088/0004-637X/794/1/58)
- Beers, T. C., Preston, G. W., & Shectman, S. A. 1985, *AJ*, 90, 2089, doi: [10.1086/113917](https://doi.org/10.1086/113917)
- . 1992, *AJ*, 103, 1987, doi: [10.1086/116207](https://doi.org/10.1086/116207)
- Beers, T. C., Placco, V. M., Carollo, D., et al. 2017, *ApJ*, 835, 81, doi: [10.3847/1538-4357/835/1/81](https://doi.org/10.3847/1538-4357/835/1/81)
- Belokurov, V., Erkal, D., Evans, N. W., Koposov, S. E., & Deason, A. J. 2018, *MNRAS*, 478, 611, doi: [10.1093/mnras/sty982](https://doi.org/10.1093/mnras/sty982)
- Belokurov, V., Sanders, J. L., Fattahi, A., et al. 2020, *MNRAS*, 494, 3880, doi: [10.1093/mnras/staa876](https://doi.org/10.1093/mnras/staa876)
- Bilir, S., Karaali, S., Ak, S., et al. 2012, *MNRAS*, 421, 3362, doi: [10.1111/j.1365-2966.2012.20561.x](https://doi.org/10.1111/j.1365-2966.2012.20561.x)
- Binney, J., & Tremaine, S. 2008, *Galactic Dynamics: Second Edition* (Princeton Series in Astrophysics)
- Binney, J., Burnett, B., Kordopatis, G., et al. 2014, *MNRAS*, 439, 1231, doi: [10.1093/mnras/stt2367](https://doi.org/10.1093/mnras/stt2367)
- Borsato, N. W., Martell, S. L., & Simpson, J. D. 2020, *MNRAS*, 492, 1370, doi: [10.1093/mnras/stz3479](https://doi.org/10.1093/mnras/stz3479)
- Campello, R. J. G. B., Moulavi, D., & Sander, J. 2013, in *Advances in Knowledge Discovery and Data Mining*, ed. J. Pei, V. S. Tseng, L. Cao, H. Motoda, & G. Xu (Berlin, Heidelberg: Springer Berlin Heidelberg), 160–172
- Carollo, D., Chiba, M., Ishigaki, M., et al. 2019, *ApJ*, 887, 22, doi: [10.3847/1538-4357/ab517c](https://doi.org/10.3847/1538-4357/ab517c)
- Christlieb, N., Schörck, T., Frebel, A., et al. 2008, *A&A*, 484, 721, doi: [10.1051/0004-6361:20078748](https://doi.org/10.1051/0004-6361:20078748)
- Coşkunoglu, B., Ak, S., Bilir, S., et al. 2012, *MNRAS*, 419, 2844, doi: [10.1111/j.1365-2966.2011.19925.x](https://doi.org/10.1111/j.1365-2966.2011.19925.x)
- . 2011, *MNRAS*, 412, 1237, doi: [10.1111/j.1365-2966.2010.17983.x](https://doi.org/10.1111/j.1365-2966.2010.17983.x)
- Cordoni, G., Da Costa, G. S., Yong, D., et al. 2021, *MNRAS*, 503, 2539, doi: [10.1093/mnras/staa3417](https://doi.org/10.1093/mnras/staa3417)
- Cui, X.-Q., Zhao, Y.-H., Chu, Y.-Q., et al. 2012, *Research in Astronomy and Astrophysics*, 12, 1197, doi: [10.1088/1674-4527/12/9/003](https://doi.org/10.1088/1674-4527/12/9/003)
- Di Matteo, P., Haywood, M., Lehnert, M. D., et al. 2019, *A&A*, 632, A4, doi: [10.1051/0004-6361/201834929](https://doi.org/10.1051/0004-6361/201834929)
- Dietz, S. E., Yoon, J., Beers, T. C., Placco, V. M., & Lee, Y. S. 2021, *ApJ*, 914, 100, doi: [10.3847/1538-4357/abefd6](https://doi.org/10.3847/1538-4357/abefd6)
- Duran, Ş., Ak, S., Bilir, S., et al. 2013, *PASA*, 30, e043, doi: [10.1017/pasa.2013.21](https://doi.org/10.1017/pasa.2013.21)
- Fulbright, J. P., Wyse, R. F. G., Ruchti, G. R., et al. 2010, *ApJL*, 724, L104, doi: [10.1088/2041-8205/724/1/L104](https://doi.org/10.1088/2041-8205/724/1/L104)
- Gaia Collaboration, Brown, A. G. A., Vallenari, A., et al. 2016a, *A&A*, 595, A2, doi: [10.1051/0004-6361/201629512](https://doi.org/10.1051/0004-6361/201629512)
- Gaia Collaboration, Prusti, T., de Bruijne, J. H. J., et al. 2016b, *A&A*, 595, A1, doi: [10.1051/0004-6361/201629272](https://doi.org/10.1051/0004-6361/201629272)
- Gaia Collaboration, Brown, A. G. A., Vallenari, A., et al. 2018, *A&A*, 616, A1, doi: [10.1051/0004-6361/201833051](https://doi.org/10.1051/0004-6361/201833051)
- . 2021, *A&A*, 649, A1, doi: [10.1051/0004-6361/202039657](https://doi.org/10.1051/0004-6361/202039657)
- Gravity Collaboration, Abuter, R., Amorim, A., et al. 2020, *A&A*, 636, L5, doi: [10.1051/0004-6361/202037813](https://doi.org/10.1051/0004-6361/202037813)
- Gudin, D., Shank, D., Beers, T. C., et al. 2021, *ApJ*, 908, 79, doi: [10.3847/1538-4357/abd7ed](https://doi.org/10.3847/1538-4357/abd7ed)
- Hayes, C. R., Majewski, S. R., Shetrone, M., et al. 2018, *ApJ*, 852, 49, doi: [10.3847/1538-4357/aa9ccc](https://doi.org/10.3847/1538-4357/aa9ccc)
- Helmi, A. 2020, *ARA&A*, 58, 205, doi: [10.1146/annurev-astro-032620-021917](https://doi.org/10.1146/annurev-astro-032620-021917)
- Helmi, A., Babusiaux, C., Koppelman, H. H., et al. 2018, *Nature*, 563, 85, doi: [10.1038/s41586-018-0625-x](https://doi.org/10.1038/s41586-018-0625-x)
- Helmi, A., & de Zeeuw, P. T. 2000, *MNRAS*, 319, 657, doi: [10.1046/j.1365-8711.2000.03895.x](https://doi.org/10.1046/j.1365-8711.2000.03895.x)
- Helmi, A., Veljanoski, J., Breddels, M. A., Tian, H., & Sales, L. V. 2017, *A&A*, 598, A58, doi: [10.1051/0004-6361/201629990](https://doi.org/10.1051/0004-6361/201629990)
- Helmi, A., White, S. D. M., de Zeeuw, P. T., & Zhao, H. 1999, *Nature*, 402, 53, doi: [10.1038/46980](https://doi.org/10.1038/46980)
- Henden, A., & Munari, U. 2014, *Contributions of the Astronomical Observatory Skalnaté Pleso*, 43, 518
- Henden, A. A., Templeton, M., Terrell, D., et al. 2016, *VizieR Online Data Catalog*, II/336
- Huang, Y., Yuan, H., Beers, T. C., & Zhang, H. 2021a, *ApJL*, 910, L5, doi: [10.3847/2041-8213/abe69a](https://doi.org/10.3847/2041-8213/abe69a)

- Huang, Y., Beers, T. C., Wolf, C., et al. 2021b, arXiv e-prints, arXiv:2104.14154, <https://arxiv.org/abs/2104.14154>
- Huang, Y., Yuan, H., Li, C., et al. 2021c, *ApJ*, 907, 68, doi: [10.3847/1538-4357/abca37](https://doi.org/10.3847/1538-4357/abca37)
- Ji, A. P., Frebel, A., Simon, J. D., & Chiti, A. 2016, *ApJ*, 830, 93, doi: [10.3847/0004-637X/830/2/93](https://doi.org/10.3847/0004-637X/830/2/93)
- Karaali, S., Bilir, S., Ak, S., et al. 2014, *PASA*, 31, e013, doi: [10.1017/pasa.2014.5](https://doi.org/10.1017/pasa.2014.5)
- Klement, R., Fuchs, B., & Rix, H. W. 2008, *ApJ*, 685, 261, doi: [10.1086/590139](https://doi.org/10.1086/590139)
- Koppelman, H., Helmi, A., & Veljanoski, J. 2018, *ApJL*, 860, L11, doi: [10.3847/2041-8213/aac882](https://doi.org/10.3847/2041-8213/aac882)
- Koppelman, H. H., Helmi, A., Massari, D., Price-Whelan, A. M., & Starkenburg, T. K. 2019a, *A&A*, 631, L9, doi: [10.1051/0004-6361/201936738](https://doi.org/10.1051/0004-6361/201936738)
- Koppelman, H. H., Helmi, A., Massari, D., Roelenga, S., & Bastian, U. 2019b, *A&A*, 625, A5, doi: [10.1051/0004-6361/201834769](https://doi.org/10.1051/0004-6361/201834769)
- Kordopatis, G., Recio-Blanco, A., Schultheis, M., & Hill, V. 2020, *A&A*, 643, A69, doi: [10.1051/0004-6361/202038686](https://doi.org/10.1051/0004-6361/202038686)
- Kordopatis, G., Gilmore, G., Steinmetz, M., et al. 2013, *AJ*, 146, 134, doi: [10.1088/0004-6256/146/5/134](https://doi.org/10.1088/0004-6256/146/5/134)
- Kunder, A., Kordopatis, G., Steinmetz, M., et al. 2017, *AJ*, 153, 75, doi: [10.3847/1538-3881/153/2/75](https://doi.org/10.3847/1538-3881/153/2/75)
- Lee, Y. S., Beers, T. C., Sivarani, T., et al. 2008, *AJ*, 136, 2022, doi: [10.1088/0004-6256/136/5/2022](https://doi.org/10.1088/0004-6256/136/5/2022)
- Li, H., Du, C., Liu, S., Donlon, T., & Newberg, H. J. 2019, *ApJ*, 874, 74, doi: [10.3847/1538-4357/ab06f4](https://doi.org/10.3847/1538-4357/ab06f4)
- Li, H., Du, C., Yang, Y., et al. 2020, *ApJ*, 895, 23, doi: [10.3847/1538-4357/ab8733](https://doi.org/10.3847/1538-4357/ab8733)
- Li, H., Tan, K., & Zhao, G. 2018, *ApJS*, 238, 16, doi: [10.3847/1538-4365/aada4a](https://doi.org/10.3847/1538-4365/aada4a)
- Limberg, G., Rossi, S., Beers, T. C., et al. 2021a, *ApJ*, 907, 10, doi: [10.3847/1538-4357/abcb87](https://doi.org/10.3847/1538-4357/abcb87)
- Limberg, G., Santucci, R. M., Rossi, S., et al. 2021b, *ApJL*, 913, L28, doi: [10.3847/2041-8213/ac0056](https://doi.org/10.3847/2041-8213/ac0056)
- . 2021c, *ApJ*, 913, 11, doi: [10.3847/1538-4357/abeefe](https://doi.org/10.3847/1538-4357/abeefe)
- Mackereth, J. T., Schiavon, R. P., Pfeffer, J., et al. 2019, *MNRAS*, 482, 3426, doi: [10.1093/mnras/sty2955](https://doi.org/10.1093/mnras/sty2955)
- Massari, D., Koppelman, H. H., & Helmi, A. 2019, *A&A*, 630, L4, doi: [10.1051/0004-6361/201936135](https://doi.org/10.1051/0004-6361/201936135)
- McMillan, P. J. 2017, *MNRAS*, 465, 76, doi: [10.1093/mnras/stw2759](https://doi.org/10.1093/mnras/stw2759)
- McMillan, P. J., & Binney, J. J. 2008, *MNRAS*, 390, 429, doi: [10.1111/j.1365-2966.2008.13767.x](https://doi.org/10.1111/j.1365-2966.2008.13767.x)
- Monty, S., Venn, K. A., Lane, J. M. M., Lokhorst, D., & Yong, D. 2020, *MNRAS*, 497, 1236, doi: [10.1093/mnras/staa1995](https://doi.org/10.1093/mnras/staa1995)
- Myeong, G. C., Evans, N. W., Belokurov, V., Amorisco, N. C., & Koposov, S. E. 2018a, *MNRAS*, 475, 1537, doi: [10.1093/mnras/stx3262](https://doi.org/10.1093/mnras/stx3262)
- Myeong, G. C., Evans, N. W., Belokurov, V., Koposov, S. E., & Sanders, J. L. 2017, *MNRAS*, 469, L78, doi: [10.1093/mnrasl/slx051](https://doi.org/10.1093/mnrasl/slx051)
- Myeong, G. C., Evans, N. W., Belokurov, V., Sanders, J. L., & Koposov, S. E. 2018b, *MNRAS*, 478, 5449, doi: [10.1093/mnras/sty1403](https://doi.org/10.1093/mnras/sty1403)
- . 2018c, *ApJL*, 856, L26, doi: [10.3847/2041-8213/aab613](https://doi.org/10.3847/2041-8213/aab613)
- Myeong, G. C., Vasiliev, E., Iorio, G., Evans, N. W., & Belokurov, V. 2019, *MNRAS*, 488, 1235, doi: [10.1093/mnras/stz1770](https://doi.org/10.1093/mnras/stz1770)
- Naidu, R. P., Conroy, C., Bonaca, A., et al. 2020, *ApJ*, 901, 48, doi: [10.3847/1538-4357/abae4f](https://doi.org/10.3847/1538-4357/abae4f)
- Onken, C. A., Wolf, C., Bessell, M. S., et al. 2019, *PASA*, 36, e033, doi: [10.1017/pasa.2019.27](https://doi.org/10.1017/pasa.2019.27)
- Placco, V. M., Frebel, A., Beers, T. C., & Stancliffe, R. J. 2014, *ApJ*, 797, 21, doi: [10.1088/0004-637X/797/1/21](https://doi.org/10.1088/0004-637X/797/1/21)
- Placco, V. M., Beers, T. C., Santucci, R. M., et al. 2018, *AJ*, 155, 256, doi: [10.3847/1538-3881/aac20c](https://doi.org/10.3847/1538-3881/aac20c)
- Rasmussen, K. C., Zepeda, J., Beers, T. C., et al. 2020, *ApJ*, 905, 20, doi: [10.3847/1538-4357/abc005](https://doi.org/10.3847/1538-4357/abc005)
- Reid, M. J., & Brunthaler, A. 2020, *ApJ*, 892, 39, doi: [10.3847/1538-4357/ab76cd](https://doi.org/10.3847/1538-4357/ab76cd)
- Rhee, J. 2001, *PASP*, 113, 1569, doi: [10.1086/324316](https://doi.org/10.1086/324316)
- Riello, M., De Angeli, F., Evans, D. W., et al. 2021, *A&A*, 649, A3, doi: [10.1051/0004-6361/202039587](https://doi.org/10.1051/0004-6361/202039587)
- Robin, A. C., Bienaymé, O., Fernández-Trincado, J. G., & Reylé, C. 2017, *A&A*, 605, A1, doi: [10.1051/0004-6361/201630217](https://doi.org/10.1051/0004-6361/201630217)
- Roederer, I. U., Hattori, K., & Valluri, M. 2018, *AJ*, 156, 179, doi: [10.3847/1538-3881/aadd9c](https://doi.org/10.3847/1538-3881/aadd9c)
- Ryu, J., & Lee, M. G. 2018, *ApJL*, 863, L38, doi: [10.3847/2041-8213/aad8b7](https://doi.org/10.3847/2041-8213/aad8b7)
- Schlafly, E. F., & Finkbeiner, D. P. 2011, *ApJ*, 737, 103, doi: [10.1088/0004-637X/737/2/103](https://doi.org/10.1088/0004-637X/737/2/103)
- Schlaufman, K. C., & Casey, A. R. 2014, *ApJ*, 797, 13, doi: [10.1088/0004-637X/797/1/13](https://doi.org/10.1088/0004-637X/797/1/13)
- Schlegel, D. J., Finkbeiner, D. P., & Davis, M. 1998, *ApJ*, 500, 525, doi: [10.1086/305772](https://doi.org/10.1086/305772)
- Schönrich, R., Binney, J., & Dehnen, W. 2010, *MNRAS*, 403, 1829, doi: [10.1111/j.1365-2966.2010.16253.x](https://doi.org/10.1111/j.1365-2966.2010.16253.x)
- Seabroke, G. M., Gilmore, G., Siebert, A., et al. 2008, *MNRAS*, 384, 11, doi: [10.1111/j.1365-2966.2007.12513.x](https://doi.org/10.1111/j.1365-2966.2007.12513.x)
- Shank, D., Beers, T. C., Placco, V. M., et al. 2021, arXiv e-prints, arXiv:2109.08600, <https://arxiv.org/abs/2109.08600>
- Steinmetz, M., Zwitter, T., Siebert, A., et al. 2006, *AJ*, 132, 1645, doi: [10.1086/506564](https://doi.org/10.1086/506564)

- Steinmetz, M., Matijević, G., Enke, H., et al. 2020a, AJ, 160, 82, doi: [10.3847/1538-3881/ab9ab9](https://doi.org/10.3847/1538-3881/ab9ab9)
- Steinmetz, M., Guiglion, G., McMillan, P. J., et al. 2020b, AJ, 160, 83, doi: [10.3847/1538-3881/ab9ab8](https://doi.org/10.3847/1538-3881/ab9ab8)
- Vasiliev, E. 2019, MNRAS, 482, 1525, doi: [10.1093/mnras/sty2672](https://doi.org/10.1093/mnras/sty2672)
- Vasiliev, E., & Baumgardt, H. 2021, MNRAS, 505, 5978, doi: [10.1093/mnras/stab1475](https://doi.org/10.1093/mnras/stab1475)
- Wolf, C., Onken, C. A., Luvaul, L. C., et al. 2018, PASA, 35, e010, doi: [10.1017/pasa.2018.5](https://doi.org/10.1017/pasa.2018.5)
- Woody, T., & Schlafman, K. C. 2021, AJ, 162, 42, doi: [10.3847/1538-3881/abff5f](https://doi.org/10.3847/1538-3881/abff5f)
- Yanny, B., Rockosi, C., Newberg, H. J., et al. 2009, AJ, 137, 4377, doi: [10.1088/0004-6256/137/5/4377](https://doi.org/10.1088/0004-6256/137/5/4377)
- Yoon, J., Beers, T. C., Placco, V. M., et al. 2016, ApJ, 833, 20, doi: [10.3847/0004-637X/833/1/20](https://doi.org/10.3847/0004-637X/833/1/20)
- York, D. G., Adelman, J., Anderson, John E., J., et al. 2000, AJ, 120, 1579, doi: [10.1086/301513](https://doi.org/10.1086/301513)
- Yuan, Z., Chang, J., Banerjee, P., et al. 2018, ApJ, 863, 26, doi: [10.3847/1538-4357/aacd0d](https://doi.org/10.3847/1538-4357/aacd0d)
- Yuan, Z., Chang, J., Beers, T. C., & Huang, Y. 2020a, ApJL, 898, L37, doi: [10.3847/2041-8213/aba49f](https://doi.org/10.3847/2041-8213/aba49f)
- Yuan, Z., Myeong, G. C., Beers, T. C., et al. 2020b, ApJ, 891, 39, doi: [10.3847/1538-4357/ab6ef7](https://doi.org/10.3847/1538-4357/ab6ef7)
- Zepeda, J., Rasmussen, K. C., Beers, T. C., et al. 2021, arXiv e-prints, arXiv:2109.13761. <https://arxiv.org/abs/2109.13761>
- Zwitter, T., Siebert, A., Munari, U., et al. 2008, AJ, 136, 421, doi: [10.1088/0004-6256/136/1/421](https://doi.org/10.1088/0004-6256/136/1/421)